

Solar Wind Proton Interactions with Lunar Magnetic Anomalies and Regolith

Charles Lue



Swedish Institute of Space Physics, Kiruna
Department of Physics, Umeå University, Umeå
2015

©Charles Lue, December 2015

Printed by Print & Media, Umeå University, Umeå, Sweden

ISBN 978-91-982951-0-8

ISSN 0284-1703

Abstract

The lunar space environment is shaped by the interaction between the Moon and the solar wind. In the present thesis, we investigate two aspects of this interaction, namely the interaction between solar wind protons and lunar crustal magnetic anomalies, and the interaction between solar wind protons and lunar regolith. We use particle sensors that were carried onboard the Chandrayaan-1 lunar orbiter to analyze solar wind protons that reflect from the Moon, including protons that capture an electron from the lunar regolith and reflect as energetic neutral atoms of hydrogen. We also employ computer simulations and use a hybrid plasma solver to expand on the results from the satellite measurements.

The observations from Chandrayaan-1 reveal that the reflection of solar wind protons from magnetic anomalies is a common phenomenon on the Moon, occurring even at relatively small anomalies that have a lateral extent of less than 100 km. At the largest magnetic anomaly cluster (with a diameter of 1000 km), an average of $\sim 10\%$ of the incoming solar wind protons are reflected to space. Our computer simulations show that these reflected proton streams significantly modify the global lunar plasma environment. The reflected protons can enter the lunar wake and impact the lunar nightside surface. They can also reach far upstream of the Moon and disturb the solar wind flow. In the local environment at a 200 km-scale magnetic anomaly, our simulations show a heated and deflected plasma flow and the formation of regions with reduced or increased proton precipitation.

We also observe solar wind protons reflected from the lunar regolith. These proton fluxes are generally lower than those from the magnetic anomalies. We find that the proton reflection efficiency from the regolith varies between $\sim 0.01\%$ and $\sim 1\%$, in correlation with changes in the solar wind speed. We link this to a velocity dependent charge-exchange process occurring when the particles leave the lunar regolith. Further, we investigate how the properties of the reflected neutral hydrogen atoms depend on the solar wind temperature. We develop a model to describe this dependence, and use this model to study the plasma precipitation on the Moon when it is in the terrestrial magnetosheath. We then use the results from these and other studies, to model solar wind reflection from the surface of the planet Mercury.

Sammanfattning

Rymdmiljön runt månen formas av den växelverkan som sker mellan månen och solvinden. I den föreliggande avhandlingen undersöker vi två aspekter av denna växelverkan, nämligen växelverkan mellan solvindsprotoner och magnetiserade områden i månskorpan, och växelverkan mellan solvindsprotoner och månens ytdamm. Vi använder oss av partikelsensorer på månsatelliten Chandrayaan-1 för att analysera solvindsprotoner som reflekteras från månen, även de protoner som fångar upp en elektron från ytan och reflekteras som neutrala väteatomer. Vi använder oss också av datorsimuleringar för att bygga vidare på de uppmätta resultaten.

Observationerna från Chandrayaan-1 visar att reflektion av solvindsprotoner från magnetiserade områden är ett vanligt förekommande fenomen på månen, som inträffar även vid magnetiseringar som är utbredda över mindre än 100 km. Vid det största magnetiserade området på månen (1000 km i diameter), reflekteras i genomsnitt $\sim 10\%$ av de infallande solvindsprotonerna. Våra datorsimuleringar visar att dessa protonflöden har globala effekter på månens plasmamiljö. De reflekterade protonerna kan nå månens nattsida. De kan också nå långt uppströms om månen och störa solvindsflödet. I den lokala plasmamiljön vid ett magnetiserat område av storleken 200 km visar våra simuleringar ett förändrat solvindsflöde, där det skapas områden som delvis skyddas från solvinden, likväl som områden som utsätts för mer solvind.

Vi observerar även solvindsprotoner som reflekterats från ytdammet på månen. Dessa protonflöden är lägre än de från de magnetiskafälten. Reflektionen från ytan varierar mellan $\sim 0.01\%$ och 1% av solvindsflödet, i samband med förändringar i solvindshastigheten. Vi förklarar detta med att partiklarnas laddning bestäms av den hastighet de har när de lämnar måndammet. Vidare undersöker vi hur egenskaperna hos de reflekterade neutrala väteatomerna beror på solvindstemperaturen. Vi skapar en modell för att beskriva sambandet och använder sedan denna modell för att studera hur solvinden faller in mot månens yta när den befinner sig i jordens magnetoskikt, där jordens magnetfält orsakar en upphettning av solvindsflödet. Resultaten från dessa och andra studier använder vi sedan för att modellera solvindsreflektion från planeten Merkurius yta, för jämförelse med framtida observationer.

List of appended papers

- Paper I:** Lue, C., Y. Futaana, S. Barabash, M. Wieser, M. Holmström, A. Bhardwaj, M. B. Dhanya, and P. Wurz (2011), Strong influence of lunar crustal fields on the solar wind flow, *Geophys. Res. Lett.*, 28, L03202, doi:10.1029/2010GL046215.
- Paper II:** Fatemi, S., M. Holmström, Y. Futaana, C. Lue, M. R. Collier, S. Barabash, and G. Stenberg (2014), Effects of protons reflected by lunar crustal magnetic fields on the global lunar plasma environment, *J. Geophys. Res. Space Physics*, 119, 8, 6095-6105, doi:10.1002/2014JA019900.
- Paper III:** Fatemi, S., C. Lue, M. Holmström, A. R. Poppe, M. Wieser, S. Barabash, and G. T. Delory (2015), Solar wind plasma interaction with Gerasimovich lunar magnetic anomaly, *J. Geophys. Res. Space Physics*, 120, 6, 4719-4735, doi:10.1002/2015JA021027.
- Paper IV:** Lue, C., Y. Futaana, S. Barabash, M. Wieser, A. Bhardwaj, and P. Wurz (2014), Chandrayaan-1 observations of backscattered solar wind protons from the lunar regolith: Dependence on the solar wind speed, *J. Geophys. Res. Planets*, 119, 5, 968-975, doi:10.1002/2013JE004582.
- Paper V:** Lue, C., Y. Futaana, S. Barabash, Y. Saito, M. Nishino, M. Wieser, K. Asamura, A. Bhardwaj, and P. Wurz (2015a), Scattering characteristics and imaging of energetic neutral atoms from the Moon in the terrestrial magnetosheath, *J. Geophys. Res. Space Physics*, under revision.
- Paper VI:** Lue, C., Y. Futaana, S. Barabash, M. Wieser, A. Bhardwaj, P. Wurz, and K. Asamura (2015b), Solar wind scattering from the surface of Mercury: Lessons from the Moon, *in preparation*.

List of related papers

- Fatemi, S., M. Holmström, Y. Futaana, S. Barabash, and **C. Lue** (2013), The lunar wake current systems, *Geophys. Res. Lett.*, *40*, 1, 17-21, doi:10.1029/2012GL054635.
- Futaana, Y., S. Barabash, M. Wieser, M. Holmström, **C. Lue**, P. Wurz, A. Schaufelberger, A. Bhardwaj, M. B. Dhanya, and K. Asamura (2012), Empirical energy spectra of neutralized solar wind protons from the lunar regolith, *J. Geophys. Res.*, *117*, E05005, doi:10.1029/2011JE00401.
- Kallio, E., R. Jarvinen, S. Dyadechkin, P. Wurz, S. Barabash, F. Alvarez, V. A. Fernandes, Y. Futaana, A.-M. Harri, J. Heilimo, **C. Lue**, J. Mäkelä, N. Porjo, W. Schmidt, and T. Siili (2012), Kinetic simulations of finite gyroradius effects in the lunar plasma environment on global, meso, and microscales, *Planet. Space Sci.*, *74*, 1, 146-155, doi:10.1016/j.pss.2012.09.012.
- Futaana, Y., S. Barabash, M. Wieser, **C. Lue**, P. Wurz, A. Vorburger, A. Bhardwaj, and K. Asamura (2013), Remote energetic neutral atom imaging of electric potential over a lunar magnetic anomaly, *Geophys. Res. Lett.*, *40*, 2, 262-266, doi:10.1002/grl.50135.
- Vorburger, A., P. Wurz, S. Barabash, M. Wieser, Y. Futaana, **C. Lue**, M. Holmström, A. Bhardwaj, M. B. Dhanya, and K. Asamura (2013), Energetic neutral atom imaging of the lunar surface, *J. Geophys. Res.*, *118*, 7, 3937-3945, doi:10.1002/jgra.50337.

Acknowledgments

I am deeply grateful for the opportunity to work with the enthusiastic and successful researchers of the Solar System Physics and Space Technology (SSPT) programme at the Swedish Institute of Space Physics in Kiruna. It has been incredible to be able to follow the ongoing research on numerous worlds in the Solar System, and the status reports for so many active and future space missions.

It has been an honor and a pleasure to study and research under the supervision of Dr. Yoshifumi Futaana and Prof. Stas Barabash. We have shared many exciting moments together, from scientific discoveries to brainstorming on physical processes or mission profiles.

I cannot imagine the SSPT group without Dr. Gabriella Stenberg Wieser, Dr. Martin Wieser, Dr. Hans Nilsson, Dr. Mats Holmström, and Dr. Masatoshi Yamauchi. It has been a great pleasure to see my friends Dr. Xiao-Dong Wang and Dr. Manabu Shimoyama join this group of scientists. You are an amazing team.

I express sincere thanks to all of Space Campus for the incredible work environment that you create.

Special thanks go to my fellow PhD students and Post-Docs, a close-knit group of friends that grows with every new PhD student that starts, but never shrinks as we part. We have had so many great experiences together in the Arctic nature and at the occasional IRF-parties. I also count other adventurous people at Space Campus to this “student” group and it is my honor to note that many reputable visitors are included here.

Last but certainly not least, I express my heartfelt gratitude to my incredibly supporting family.

Table of contents

Abstract	iii
Sammanfattning	iv
List of appended papers	v
List of related papers	vi
Acknowledgments.....	vii
1. The solar wind and the Moon	1
1.1 The solar wind	1
1.2 Planetary interactions with the solar wind.....	2
1.2.1 Intrinsic magnetospheres.....	3
1.2.2 Induced magnetospheres.....	3
1.2.3 Comet-type interaction	4
1.2.4 Moon-type interaction	4
1.3 The cis-lunar plasma environment	5
1.3.1 The solar wind near the Earth	6
1.3.2 The terrestrial foreshock region.....	6
1.3.3 The terrestrial magnetosheath	7
1.3.4 The terrestrial magnetotail	7
1.4 The Moon	8
1.4.1 The lunar interior	8
1.4.2 The lunar magnetic anomalies	9
1.4.3 The lunar regolith	9
1.4.4 The lunar exosphere.....	10
1.5 The lunar plasma environment	11
1.5.1 The classic view of the lunar plasma environment	11
1.5.2 New views of the lunar plasma environment	13
2. Instrumentation, data, and models	15
2.1 Chandrayaan-1	15
2.1.1 Orbit and attitude	16

2.1.2	The SARA instrument	17
2.1.3	The SWIM ion sensor	19
2.1.4	The CENA neutral atom sensor	19
2.2	Upstream references	21
2.2.1	Wind plasma data	21
2.2.2	Kaguya plasma data	22
2.3	Selenographical references	23
2.3.1	Clementine lunar albedo map	23
2.3.2	Lunar Prospector empirical crustal field model	23
2.4	Hybrid simulations	24
2.7.1	General principles	25
2.7.2	The FLASH hybrid code.....	25
3.	Proton interactions with lunar magnetic anomalies	27
3.1	Plasma interactions with magnetic fields	27
3.1.1	Fundamental laws of electrodynamics.....	27
3.1.2	Boundaries and pressure balance	28
3.2	Proton dynamics at crustal magnetic anomalies.....	29
3.2.1	Mini-magnetospheres and sub-magnetospheric interactions	30
3.2.2	Proton deceleration and deflection	31
3.2.3	Proton heating and reflection	32
3.3	Implications of the solar wind interaction with lunar magnetic anomalies.....	32
3.3.1	Effects on the local environment	32
3.3.2	Effects on the local surface evolution	32
3.3.3	Effects on the global environment	33
4.	Proton interactions with lunar regolith	35
4.1	Particle-surface interactions.....	35
4.1.1	Basic concepts	35
4.1.2	Collisions and particle movement in a solid material	36

4.1.3	Charge-exchange processes	37
4.2	Proton scattering from regolith	38
4.2.1	Charge states	38
4.2.2	Scattering rate	39
4.2.3	Scattering function	39
4.2.4	Energy spectrum	39
4.3	Implications of the solar wind interaction with regolith	40
4.3.1	Effects on the plasma environment	40
4.3.2	Effects on the volatiles budget	41
4.3.3	Remote-sensing applications	41
5.	Summary of papers	43
	Paper I	43
	Paper II	43
	Paper III	44
	Paper IV	44
	Paper V	45
	Paper VI	45
	References	47

1. The solar wind and the Moon

The Sun continuously emits a supersonic flow of plasma called the solar wind. The solar wind interacts with the planets and other objects in the Solar System and plays an important role in shaping planetary plasma environments, modifying the exchange of material between planets and space, and affecting planetary evolution.

An initial picture of the solar wind interaction with the Moon started to form with the Explorer, Luna, and Apollo programs. In this picture, the Moon is portrayed as a passive absorber of the solar wind, forming a plasma void downstream. However, there are also many observations of lunar plasma phenomena that cannot be explained by this classical picture.

Here, we introduce the basic properties of the solar wind, the Moon, and the lunar plasma environment.

1.1 The solar wind

Before the first satellites, the existence of the solar wind as a stream of ions and electrons from the Sun was predicted based on its measurable effects on the Earth [Chapman and Ferraro, 1930] and on cometary tails [Biermann, 1951]. The existence was later confirmed by the Luna 2 [Gringauz *et al.*, 1961] and Explorer 10 [Bridge *et al.*, 1962] satellites, recording positive ion fluxes between 10^8 and $10^9 \text{ cm}^{-2}\text{s}^{-1}$, at energies around 1 keV (corresponding to speeds around 450 km/s).

The solar wind composition was found to be mainly of protons (H^+) and electrons (e^-), with a few percent of alpha particles (He^{++}) and smaller fractions of heavier ions (Table 1).

As the solar wind plasma flows away from the Sun, it carries with it the solar magnetic field, as predicted by [Alfvén, 1957], thus forming the interplanetary magnetic field (IMF). The field is shaped into a spiral due to the rotation of the Sun [Parker, 1958; 1963] (Figure 1).

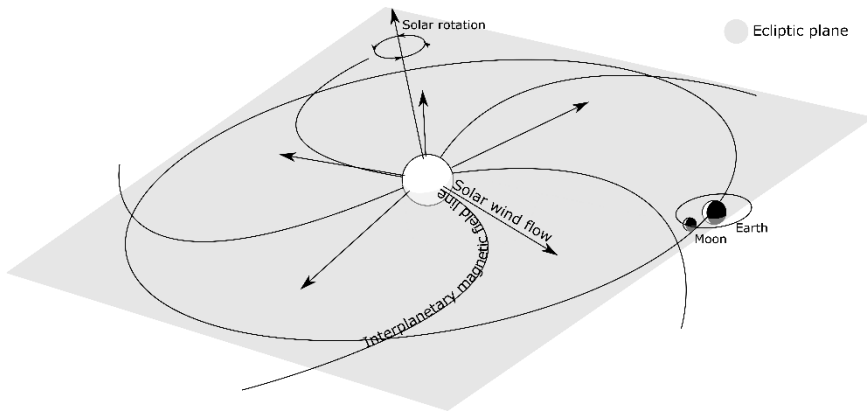


Figure 1 – An illustration of the expansion of the solar wind and the interplanetary magnetic field, showing only the ecliptic plane. Adapted from *Parker [1963]*. Not to scale.

Table 1 – Abundances [*Bochsler, 2000*] and charge states [*Snowden et al., 2004*] of the five lightest elements in the solar wind.

Element	Fraction (Interstream)	Fraction (Coronal hole)	Dominant charge states
H	0.97	0.96	H ⁺
He	$3 \cdot 10^{-2}$	$4 \cdot 10^{-2}$	He ⁺²
C	$2 \cdot 10^{-4}$	$5 \cdot 10^{-4}$	C ⁺⁵ – C ⁺⁶
O	$4 \cdot 10^{-4}$	$7 \cdot 10^{-4}$	O ⁺⁶ – O ⁺⁷
Ne	$6 \cdot 10^{-5}$	$1 \cdot 10^{-4}$	Ne ⁺⁸

1.2 Planetary interactions with the solar wind

A planetary object’s interaction with the solar wind can be very different depending on the properties of the object. Here, we introduce four classes of planetary interactions with the solar wind: Intrinsic magnetospheres, induced magnetospheres, comet-type interaction and Moon-type interaction. Note that this is a generalization and the actual interaction can differ greatly between different objects of each class, as well as for the same object at different times. Objects may also exhibit interaction types belonging to multiple classes, such as comet-like interactions at Mars [*Holmström and Wang, 2015*] and the Moon [*Halekas et al., 2012*]; Moon-like surface interactions at Mercury [*Lue et al., 2015b*]; mini-magnetospheres at asteroids [*Omidi et al., 2002*], the Moon [*e.g., Lin et al., 1998*], and Mars [*Harnett and Winglee, 2003b*]; and induced magnetic fields at the Moon [*e.g., Fatemi et al., 2015b*].

1.2.1 *Intrinsic magnetospheres*

Because the solar wind consists of charged particles, it strongly interacts with planetary magnetic fields. Planets with a strong intrinsic magnetic moment, such as the Earth, therefore interact with the solar wind already at great distances from the planet. The terrestrial magnetopause (see also Section 1.4) is the boundary where the solar wind pressure is balanced by the pressure from the terrestrial magnetic field. At the sub-solar point, the Earth-magnetopause distance is ~ 10 Earth radii (R_E) [e.g., Fairfield, 1971; Shue *et al.*, 1997]. This boundary is sensed by the solar wind even further upstream, at the terrestrial bow shock, at $\sim 15 R_E$ [e.g., Fairfield, 1971], where the solar wind starts to become compressed, heated, and deflected. Downstream, the magnetopause extends to great distances (~ 100 - $200 R_E$), forming the terrestrial magnetotail [e.g., Ness, 1969].

Although the planetary magnetic field deflects much of the solar wind flow, it does not inhibit solar wind precipitation. The cusps that form where the terrestrial magnetic field reconnects with the IMF allow the solar wind plasma to enter (and planetary ions to escape) through the magnetopause. Additionally, plasma is captured by the stretched magnetotail, into the plasma sheet, which precipitates in the auroral oval. [e.g., Russell, 1995]

Similar morphologies and processes are observed at the giant planets and Mercury, although there are also great differences between them, such as the active moons and rapid rotation rate of the Jovian and Kronian magnetospheres, the tilted Uranian rotation axis, the tilted Neptunian magnetic dipole axis, and lack of a Hermean atmosphere. [e.g., Russell, 1995]

1.2.2 *Induced magnetospheres*

Mars and Venus do not have any significant intrinsic magnetic field. However, the solar wind still doesn't directly impact their atmospheres. This is because the upper layers of these atmospheres are ionized (ionospheres). Behaving as conductive shells around the planets, the ionospheres will host induced currents in response to any magnetic field variations, and effectively create an induced magnetic field that inhibits diffusion of the IMF and thereby also the solar wind into the ionosphere. Similarly to the terrestrial magnetopause, this boundary gives rise to an upstream bow shock and a downstream magnetotail, including the formation of a plasma sheet, although the convection in these plasma sheets is mainly downstream, carrying away planetary ions rather than returning planetary and solar wind ions. [e.g., Luhmann, 1995]

1.2.3 Comet-type interaction

Planetary objects with an atmosphere but a low gravity form extended exospheres (i.e. uncollisional atmospheres), such as the comae of active comets, rather than a confined ionosphere dense enough to create an induced magnetosphere and hold off the solar wind. Instead, the cometary ions and the solar wind overlap. In this situation, the cometary ions will become accelerated (picked up) by the solar wind. In return, the solar wind is decelerated and deflected. The deceleration effect is called mass-loading of the solar wind. As the mass-loaded solar wind flows slower than the surrounding solar wind, a draping and pile-up of the IMF occurs. The IMF can be sufficiently piled-up to restrict the solar wind plasma flow, creating a plasma void. However, if the coma is small compared to the gyro-radius of the cometary ions, the solar wind will be significantly deflected in the direction opposite to the pick-up acceleration of the cometary ions rather than being deflected by a pile-up boundary [Behar *et al.*, 2015]. If a pile-up boundary forms, or if the solar wind is slowed to subsonic speeds, a bow shock may form around or near the comet. [e.g., Luhmann, 1995]

1.2.4 Moon-type interaction

The Moon, the Martian moons Phobos and Deimos, and many of the asteroids are examples of Solar System objects with a thin enough exosphere and weak enough magnetic field that the solar wind primarily interacts with the surface. The interaction is characterized by absorption and, for the Moon and large asteroids, the formation of a wake and a rarefaction region that supplies plasma to refill the wake [e.g., Luhmann, 1995]. The smaller objects in this class (smaller than the gyro-radius of solar wind protons) create very little shadowing of the solar wind in their wake, which is quickly filled-in.

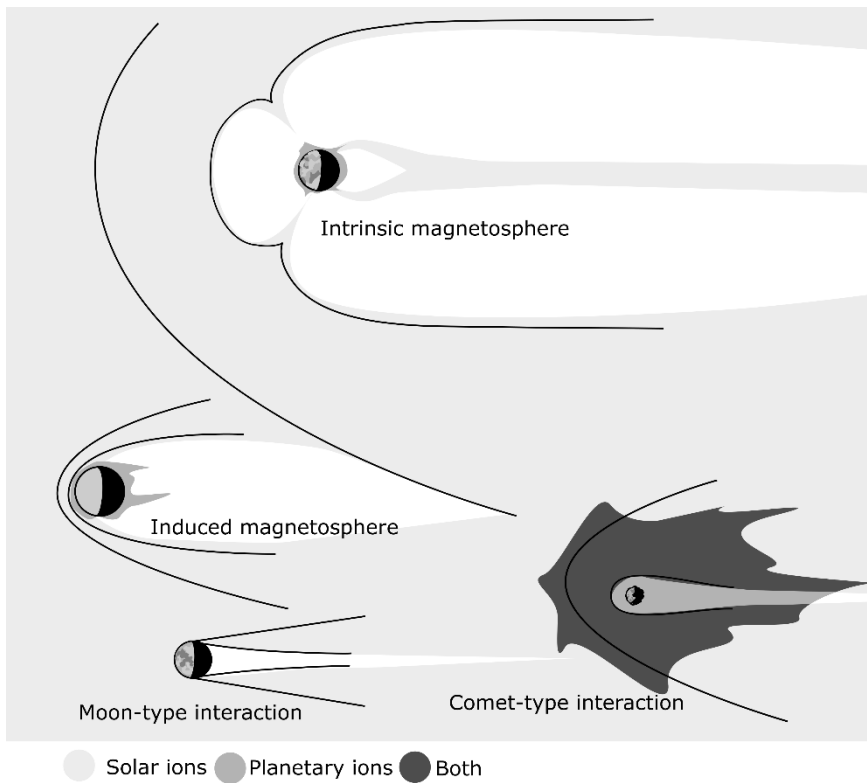


Figure 2 – An overview of different classes of planetary interactions with the solar wind. The black lines indicate the main interaction boundaries (see text).

1.3 The cis-lunar plasma environment

The external plasma environment that the Moon is exposed to is not only the undisturbed solar wind. The Moon also passes through the wake of the Earth each month. Figure 3 shows an overview of the Moon-Earth system and the main plasma domains in the space between the Earth and the lunar orbit, referred to as cis-lunar space. The interaction boundaries of the solar wind-Earth interaction were introduced in Section 1.2.1: the magnetopause and the bow shock. The region of shocked solar wind between these boundaries is called the magnetosheath. The region within the magnetopause in the wake, is the magnetotail. The magnetotail consists of two lobes which has much less plasma than the surrounding regions, separated by the plasma sheet in the equatorial plane. The region outside the bow shock consists mainly of undisturbed solar wind, with the exception of certain foreshock effects.

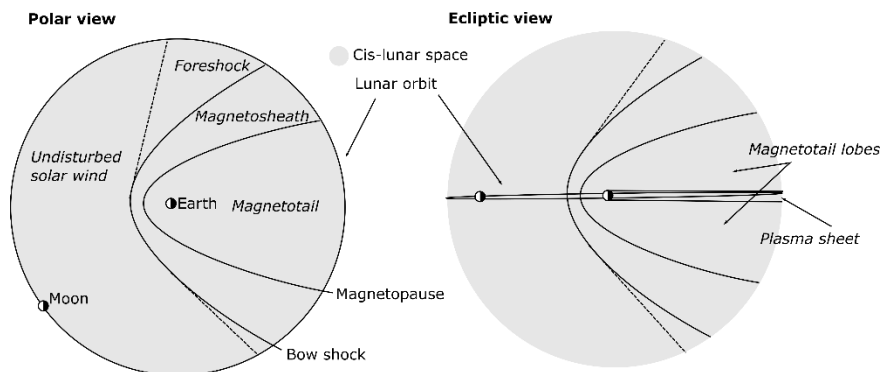


Figure 3 – The plasma regions encountered by the Moon in its orbit. The Moon and the Earth are not to scale. The extent of the foreshock region varies greatly depending on the upstream conditions.

1.3.1 The solar wind near the Earth

Typical values for the solar wind parameters just upstream of the Earth are listed in Table 2. Note that although the proton and electron densities are different, the total charge density is zero; He⁺⁺ and heavier, multiply charged ions (Table 1) hold the remaining positive charge. The proton motion is dominated by the bulk speed, while the electron motion is dominated by its thermal speed.

Table 2 - Typical solar wind parameters at the orbit of the Earth [Hundhausen, 1995].

Quantity	Value	Note
Proton density	6.6 cm^{-3}	
Electron density	7.1 cm^{-3}	
Bulk speed	450 km/s	i.e. 1 keV proton energy
Proton temperature	10 eV	i.e. 45 km/s thermal speed
Electron temperature	12 eV	i.e. 2100 km/s thermal speed

1.3.2 The terrestrial foreshock region

The region outside the bow shock is not completely undisturbed. Some of the particles encountering the bow shock are reflected from the shock, forming a region called the foreshock [e.g., Eastwood *et al.*, 2005]. The bow shock-reflected solar wind protons become picked-up and accelerated by the bulk solar wind. In their resulting cycloid motion, these protons can reach several keV (at most up to three times the solar wind velocity; i.e. up to 1400 km/s, or 10 keV, for typical solar wind speeds). The foreshock protons were first observed by the Vela

satellites [Asbridge *et al.*, 1968], reporting densities of these protons up to 10%, but typically ~1% or less, of the solar wind density, and energies of 3-6 keV.

Such accelerated protons have also been observed on the lunar surface by Apollo instruments [Benson *et al.*, 1975b], at energies of ~750-3500 eV, where 3500 eV was the instrumental upper limit. Correlations were found to the position of the Moon in relation to the bow shock, and the direction of the IMF (which determines the pick-up trajectory). The directional fluxes of these protons at the Moon were on the order of $10^5 \text{ cm}^{-2}\text{-s}^{-1}\text{sr}^{-1}$. For a discussion on the presence and role of foreshock electrons in the lunar environment, see Collier *et al.* [2011].

1.3.3 *The terrestrial magnetosheath*

The magnetosheath consists of solar wind that has passed through the terrestrial bow shock. The region is caused by the pile-up and deflection that the magnetopause enforces on the solar wind. Consequently, the plasma here is heated (to 40-400 eV), compressed (to $2\text{-}50 \text{ cm}^{-3}$), and decelerated (to 200-500 km/s). [Frank, 1985, and references therein]. In this region, the solar wind thermal distribution also changes from a normal statistical distribution (shifted Maxwellian) to a distribution with significant tails towards higher thermal velocities (typically described by a shifted kappa distribution, with a kappa value around 2 [Formisano *et al.*, 1973]).

The Apollo plasma instruments were well situated to study the magnetosheath plasma, and contributed to the characterization of this region. Clay *et al.*, [1975] reported average magnetosheath parameters of ~350 km/s bulk speed, ~100 km/s thermal speed (~50 eV) and $\sim 10 \text{ cm}^{-3}$ proton density, using Apollo 12 and 15 surface instruments.

1.3.4 *The terrestrial magnetotail*

The magnetotail is the region that is inside of the magnetopause and downstream of the Earth. It contains several sub-regions [e.g, Frank, 1985]. The boundary layer is the outer shell of the magnetotail, bordering the magnetosheath. The part of the boundary layer that the Moon encounters is the low-latitude boundary layer. It contains a mixture of plasma of magnetosheath and plasma sheet origin, and its plasma properties lie between the values of those regions. Further in are the northern and southern magnetotail lobes, containing very little plasma, and between them, the equatorial layer filled by tenuous ($0.1\text{-}1 \text{ cm}^{-3}$) but hot (400-4000 eV) plasma called the plasma sheet, with highly variable bulk velocities (10-1000 km/s) [Frank, 1985, and references therein].

When the Moon is in the magnetotail, it can be located either in one of the tail lobes, or in the plasma sheet. *Rich et al.* [1973] used Apollo 14 surface plasma measurements to estimate the probability of encountering the plasma sheet to 10%-70%, varying with the geomagnetic activity. They also characterized the plasma sheet at the lunar orbit, giving densities of $0.05\text{-}0.2\text{ cm}^{-2}$ and ion temperatures of 1-5 keV.

1.4 The Moon

The Moon has a tenuous, uncollissional atmosphere, i.e., an exosphere, and no internal dynamo capable of generating a global magnetic field. Instead, the solar wind interacts directly with the lunar surface regolith, or with patches of permanent crustal magnetic anomalies. In this section, we briefly describe the current understanding of the lunar interior, surface, and exosphere.

1.4.1 The lunar interior

A comprehensive review of the lunar interior is given by *Wieczorek et al.* [2006]. Figure 4 shows the estimated solid and liquid core radii, based largely on Apollo-era surface instruments [e.g., *Hood*, 1986] and early mantle evolution models [*Smith et al.*, 1970; *Wood et al.*, 1970], together with the results of more recent satellite mapping missions [e.g., *Lawrence et al.*, 1998].

Although the Moon likely still has a liquid lunar core, there is apparently not enough convective motion in it to create a significant magnetic dynamo. Based on Apollo 15 and Apollo 16 Plasma and Fields Subsatellites PFS-1 and PFS-2, an upper limit of the intrinsic dipole moment was given as $4.4 \cdot 10^{10}\text{ Am}^2$ [*Dyal et al.*, 1974].

Nevertheless, the core is expected to be conductive, and can create an induced magnetic field to prevent IMF diffusion through the core. *Dyal et al.* [1974] calculated the typical induced dipole moment to $2 \cdot 10^{15}\text{ Am}^2$ (much higher than the aforementioned dipole moment). Assuming an induced magnetic moment of 10^{16} Am^2 , corresponding to an IMF change of 25 nT according to Apollo estimates of the induced magnetic moment ($-4 \cdot 10^{14}\text{ Am}^2/\text{nT}$) [*Russell et al.*, 1974; 1981], which is compatible with a conductive core of $\sim 400\text{ km}$ radius, *Fatemi et al.* [2015b] found that this induced field could alter the total magnetic field amplitude in the lunar wake by up to 10%. However, in most conditions, the induced field will not play a significant role in the solar wind-Moon interaction.

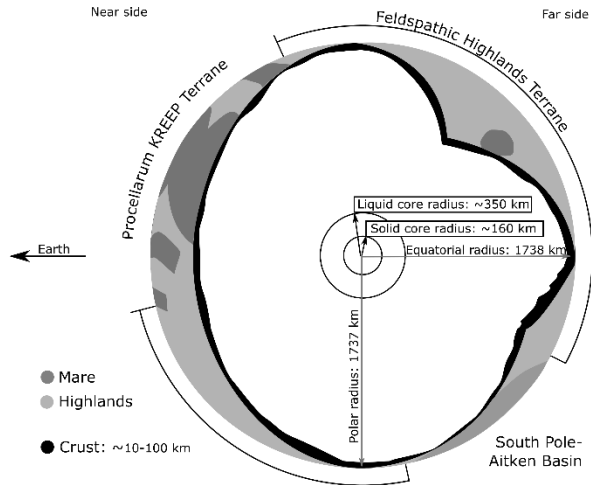


Figure 4 – Overview of the lunar interior and terrane. Adapted from *Wieczorek et al.* [2006].

1.4.2 The lunar magnetic anomalies

The most noticeable lunar magnetic field is that from the regions of permanently magnetized crust, the lunar magnetic anomalies. The lunar magnetic anomalies were discovered by the Apollo 12 magnetometer deployed on the lunar surface [Dyal et al., 1970] and by Explorer 35 from orbit [Mihalov et al., 1971].

It was soon proposed that the magnetic anomalies could be responsible for disturbances of the solar wind near the lunar limb, although it was argued that the Apollo 12 field was not strong enough for significant solar wind disturbances [Barnes et al., 1971]. The surface fields measured by Apollo 12, 14, 15, and 16 magnetometers were 38, 103, 3, and 327 nT, respectively [Dyal et al., 1974]. While the Apollo landing sites were all on the lunar near side, satellite observations showed that the largest and strongest magnetic fields, responsible for most of the solar wind limb disturbances were located on the lunar far side [e.g., Coleman et al., 1972].

1.4.3 The lunar regolith

The lunar surface is covered by a layer of fine-grained dust. This is called the lunar regolith. The composition of the regolith reflects the composition of the lunar crust, consisting mainly of silicate rock. However, the regolith properties are also highly determined by space weathering processes. Exposure of the crust material to micrometeorite impacts, solar wind particles, cosmic ray particles, and solar photons is responsible for forming and modifying the regolith. This space weathering turns the rock of the upper crust into a porous layer of glassy,

irregularly shaped, sharp, abrasive, chemically reduced, micrometer-sized grains. In fact, it is very difficult to reproduce the complete properties of lunar regolith on Earth [e.g., *Taylor and Liu, 2010*].

There are selenographic differences in regolith thickness and grain composition, likely due to large-scale differences in the lunar mantle and crust evolution, including resurfacing by large meteorite impacts [e.g., *Wieczorek et al., 2006*, and references therein]. The lunar topography is commonly divided in two types of terrain: the smoother, fresher Mare regions, and the rougher, older Highland regions. Alternatively, three main *terrane*, focused more on compositional differences are defined [*Joliff et al., 2000*]: the Procellarum KREEP Terrane; the Feldspathic Highlands Terrane; and the South Pole-Aitken Terrane. (See Figure 4.)

The majority of the solar wind becomes absorbed in the lunar regolith and then outgasses into the lunar exosphere (e.g. as hydrogen molecules). However, recent studies have found that 10%-20% of the solar wind protons reflect off the surface as energetic neutral hydrogen atoms [*McComas et al., 2009*; *Wieser et al., 2009*], and ~0.1%-1% as reflected protons [*Saito et al., 2008*].

1.4.4 The lunar exosphere

Hinton and Tausch [1964] made a theoretical model of the lunar exosphere by considering the source rates from the solar wind and internal lunar sources, assuming similar internal radiogenic release as on the Earth. The resulting density (of mainly argon and neon) for typical solar wind conditions was $\sim 10^5 \text{ cm}^{-3}$. *Johnson et al.* [1972], using Apollo surface instruments, measured the density to $2 \cdot 10^5 \text{ cm}^{-3}$ (at sunset), and assumed neon to be the main component [*Johnson et al., 1971*]. This value was supported by observations of the exo-ionosphere of 2 cm^{-3} [*Freeman et al., 1973*] (assuming the ionized fraction to be 10^{-5} [*Johnson et al., 1971*]).

Stern [1999] reviewed the observations of the lunar exosphere from Apollo, ground-based, and Hubble observations. They listed the likely main constituents of the lunar exosphere, excluding neon due to ambiguities in detecting it. Argon is primarily produced by radioactive decay in the Moon, while helium is mainly of solar wind origin. The near-surface densities tend to increase at night because of lower temperatures and thus lower atmospheric scale height. For argon on the other hand, the nightside temperatures are sufficient to cause condensation on the lunar surface, thus reducing the nightside argon exosphere [*Stern, 1999*]. Recent observations of the lunar exosphere by instruments on the Lunar Reconnaissance Orbiter (LRO) [*Stern et al., 2013*] and the Lunar Atmosphere and Dust Environment Explorer (LADEE) [*Benna et al., 2015*] have updated the picture

with more details on the spatial distribution as well as composition of the exosphere, including a characterization of the neon component [Benna *et al.*, 2015].

Table 3 – Lunar surface exospheric densities for some of the most common and best studied species. See also Stern [1999] for a larger number of species.

Species	Number density [cm ⁻³]	Reference
Ar	10 ³ (pre-sunrise) – 10 ⁵ (sunrise)	Benna <i>et al.</i> [2015]
Ne	<10 ³ (day) – 3·10 ⁴ (pre-sunrise)	Benna <i>et al.</i> [2015]
He	<10 ³ (day) – ~3·10 ⁴ (night)	Benna <i>et al.</i> [2015]
CH ₄	10 ⁴ (pre-sunrise)	Hodges and Hoffman [1975]
H ₂	1·10 ³ (day, night)	Stern <i>et al.</i> [2013]

The species of the lunar exosphere become ionized by the solar radiation. This can be called an exo-ionosphere. For number densities of ~2 cm⁻³ [Freeman *et al.*, 1973] at thermal velocities, the effect of these ions on the solar wind flow is small. However, in addition to the exo-ionosphere there is a layer of photo-electrons, emitted from the surface by solar UV radiation. The density of this photo-electron layer decreases rapidly with height, from 10⁴ cm⁻³ at 1 cm, to 10² cm⁻³ at 1 m, and 1 cm⁻³ at a few km [Reasoner and Burke, 1972]. In addition, there may be a component of dust in the exosphere. The dynamics of these Moon-originating components of the lunar plasma environment were discussed by *e.g.*, Stubbs *et al.* [2006]; Halekas *et al.* [2011]; Kallio *et al.* [2012]. The photoelectron energies determine the lunar dayside surface potential as it charges to several volts until most of the photoelectrons are returned to the surface, achieving current balance.

1.5 The lunar plasma environment

The lunar plasma environment is a result of the upstream environment, the lunar properties, and the interaction mechanisms. However, the current view of the lunar environment is to a large extent based on empirics rather than an understanding of these conditions. In this section, the global view of the lunar plasma environment is reviewed. The experimental data sets have been greatly expanded with recent orbiter missions. Computer models are also increasingly capable of explaining and expanding on the observed results.

1.5.1 The classic view of the lunar plasma environment

The early lunar missions, Luna 2 [Dolginov *et al.*, 1961] and Explorer 35 [Ness *et al.*, 1967; Sonett *et al.*, 1967] found no indication of any significant intrinsic or induced lunar magnetic field, but only a diamagnetic cavity consistent with a

plasma void in the lunar wake [Colburn *et al.*, 1967], as confirmed by particle measurements [Lyon *et al.*, 1967].

Thus, the initial picture of the Moon-solar wind interaction is one of a solar wind-absorbing, resistive, unmagnetized sphere. In this picture, the solar wind is undisturbed upstream of the Moon, and a void is formed behind the Moon. As the solar wind flow is supersonic it can only begin to refill the void from a region bounded by a so-called rarefaction wave [Spreiter *et al.*, 1970].

This picture is less simple to model than one can imagine. The early model by Spreiter *et al.* [1970] assumed a gas-like expansion into the wake of a supersonic object. More recently, Wang *et al.* [2011], Wiehle *et al.* [2011], and Holmström *et al.* [2012] used hybrid (ions as particles and electrons as a fluid) computer simulations to model the solar wind-Moon interaction, for different orientations of the IMF, and identified several regions of the lunar wake. The result from Holmström *et al.* [2012] is shown in Figure 5. The simulations show an initial refilling of the void from the rarefaction region. The refilling plasma compresses the magnetic field in the void until the field is strong enough to hold off the refilling plasma. This happens at a few lunar radii downstream. There, a recompression wave forms, where the refilling plasma is compressed against the void boundary, forming a region denser than the upstream solar wind. After this point of pressure balance, the refilling of the void continues mainly by diffusion along the IMF, forming a cylindrically assymmetric, second rarefaction region that is interior to the radius of the compression wave. For an investigation of the current systems related to these simulations, see Fatemi *et al.* [2013].

The main regions of the wake (a rarefaction region, a void, and possibly a recompression wave) were supported by observations by e.g., the Wind spacecraft [Bosqued *et al.*, 1996; Ogilvie *et al.*, 1996] and the Acceleration, Reconnection, Turbulence, and Electrodynamics of the Moon's Interaction with the Sun (ARTEMIS) spacecraft [Wiehle *et al.*, 2011], but certain details were clearly different, such as the central wake density [Holmström *et al.*, 2012]. These differences may be due to the disturbances discussed in the next section.

Although we know that there are disturbances to this picture in reality, those disturbances can be variable and sporadic. Thus, the picture may still be valid for some upstream conditions. Complementing the hybrid models, Halekas *et al.* [2014] showed that a one-dimensional analytical model for plasma diffusion into the wake sometimes reproduced ARTEMIS observations remarkably well, though they noted large differences at other times. Regardless of its applicability to the real Moon, the picture presented in this sub-section is important for

understanding and predicting interactions between plasma and atmosphereless objects in general.

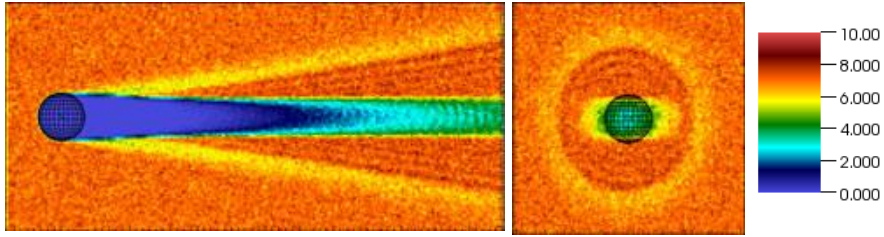


Figure 5 – Solar wind interaction with a resistive, unmagnetized and absorbing Moon. Reprinted from *Holmström et al.* [2012]. The colorscale shows the proton number density in cm^{-3} . The IMF is along (1, 1, 0) in the Selenocentric Solar Ecliptic coordinate system, the left panel shows the x-z plane and the right panel shows the y-z plane, in a cut near the right edge of the picture in the left panel.

1.5.2 New views of the lunar plasma environment

In the picture discussed above, the solar wind is undisturbed upstream of the rarefaction wave. However, lunar satellites found strong perturbations of the magnetic field and plasma near the lunar day-night terminator, referred to as limb shocks or limb compressions [e.g., *Ness et al.*, 1968; *Barnes et al.*, 1971; *Colburn et al.*, 1971]. The occurrence of these perturbations showed a correlation with the proximity of lunar magnetic anomalies to the terminator region [*Criswell*, 1972; *Neugebauer et al.*, 1972; *Russell and Lichtenstein*, 1975].

Additionally, the picture does not allow significant plasma entry deep into the near-Moon wake. Nevertheless, protons were found impacting the lunar surface deep inside the wake [*Freeman*, 1972]. Recent orbital missions at low altitudes confirmed the common occurrence of protons in the near-Moon, deep wake [*Nishino et al.*, 2009; *Futaana et al.*, 2010; *Dhanya et al.*, 2013].

Even in the upstream solar wind at thousands km away from the Moon, stray proton populations were observed, apparently traveling from the Moon [*Futaana et al.*, 2003].

An important clue to explaining these proton streams came when proton reflection from the lunar surface (at 0.1%-1%) was detected by Kaguya [*Saito et al.*, 2008]. Contrary to electrons, reflected protons have large gyroradii in the lunar environment, comparable to the lunar radius. Thus, they can reach both upstream of- and around the Moon, into the wake. Significant proton reflection from the Moon was also confirmed by observations by the Chandrayaan-1 [*Holmström et al.*, 2010] and Chang'e-1 [*Wang et al.* 2010] spacecraft. Modeling

of the resulting proton trajectories showed that reflected protons with the observed characteristics indeed could reach the upstream and downstream locations where previous observations had been reported [e.g., *Holmström et al.*, 2010]. The picture was further changed when *Saito et al.* [2010] showed that the lunar magnetic anomalies contributed to the proton reflection, locally causing a much stronger ($>10\%$) reflection.

The changes to our view of the lunar environment on the basis of these and a range of similar phenomena, such as plasma waves [e.g., *Kellogg et al.*, 1996; *Nakagawa et al.*, 2003]; electron-surface interactions and surface charging [e.g., *Halekas et al.*, 2009]; and electrostatic dust lofting [e.g. *Stubbs et al.*, 2006] were discussed by *Halekas et al.* [2011], and is summarized in Figure 6. The view that is taking shape is one of a highly dynamic lunar plasma environment. Some of the advances to this picture from the last five years, and the ongoing research on this topic will be presented in Chapter 3 and 4, and in the appended papers.

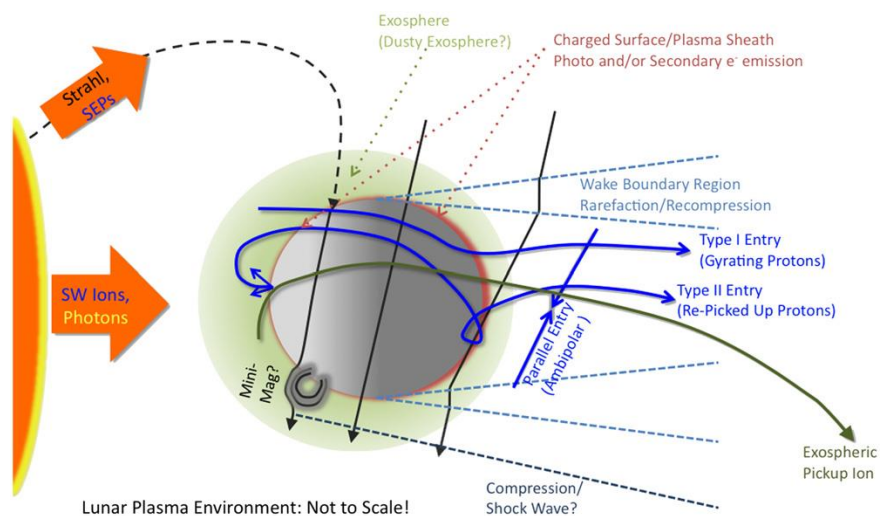


Figure 6 – An overview of the dynamic lunar plasma environment. Reprinted from *Halekas et al.* [2011] with permission from Elsevier.

2. Instrumentation, data, and models

In this thesis, we present spacecraft observations as well as computer simulations. The main data set analyzed is that of the Sub-keV Atoms Reflecting Analyzer (SARA) on the lunar orbiter Chandrayaan-1. In addition to this data set, several sources of supplementary data have been crucial for putting the observations in their proper context. We also use computer simulations that run the FLASH hybrid plasma solver.

2.1 Chandrayaan-1

Chandrayaan-1 [Goswami and Annadurai, 2008] was launched in October 2008, as the first Indian lunar mission. The mission was aimed primarily at geological studies of the lunar surface. It carried a range of spectrometers and cameras (Table 4; Figure 7). From a low-altitude polar lunar orbit, these instruments allowed global mapping of surface properties.

The surface evolution and the retention of volatiles are strongly coupled to the lunar environment. Chandrayaan-1 carried an impact probe to measure the lunar exosphere, a radiation monitor for high-energy particles (cosmic rays), and SARA, a low-energy particle instrument studying particle emissions from the surface and solar wind precipitation.

Table 4 – Instrumentation on Chandrayaan-1 [Goswami and Annadurai, 2008].

Instrument	Full name	Objective
C1XS	Chandrayaan-1 X-ray Spectrometer	Elemental mapping
HEX	High-Energy X-γ ray Spectrometer	Volatiles mapping
HySI	Hyper-Spectral Imager	Mineralogical mapping
LLRI	Lunar Laser Ranging Instrument	Topographical mapping
M ³	Moon Mineralogy Mapper	Mineralogical mapping
Mini-SAR	Miniature Synthetic Aperture Radar	Water ice mapping
MIP	Moon Impact Probe	Exosphere
RADOM	Radiation Dose Monitor	Radiation environment
SARA	Sub-keV Atoms Reflecting Analyzer	Solar wind interaction
SIR-2	Spectrometer Infrared 2	Mineralogical mapping
TMC	Terrain Mapping Camera	Topographical mapping

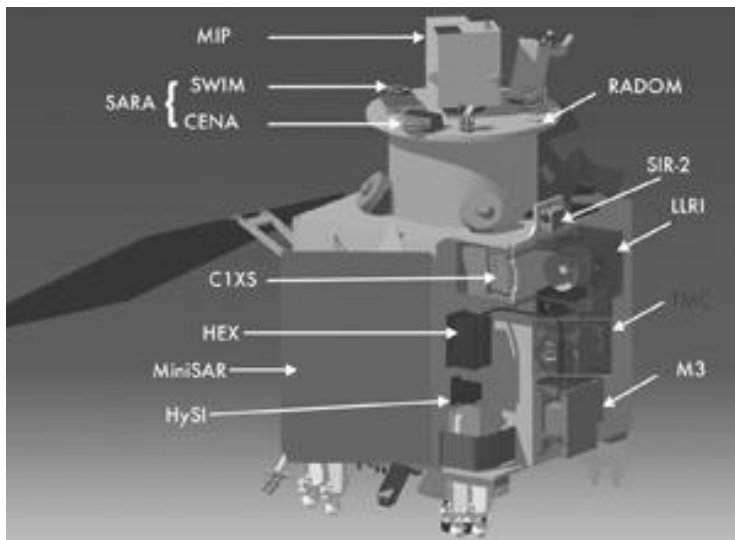


Figure 7 – The Chandrayaan-1 spacecraft. Image credit: ISRO.

2.1.1 Orbit and attitude

As required for global mapping, Chandrayaan-1 was inserted into a polar orbit. The spacecraft was also three-axis stabilized to keep mapping instruments surface-pointed. The nominal orbit altitude was 100 km, corresponding to an orbital period of 118 minutes. On 26 April 2009, the altitude was raised to 200 km (128 minutes).

Due to the motion of the Moon (and the Earth) around the Sun, the spacecraft orbital plane in the Moon-Sun reference frame precessed with $\sim 1^\circ$ per day (Figure 8). Thus, the orbit moved from noon-midnight alignment to terminator alignment over three months. The first SARA data were retrieved in December, 2008, and the nominal science operations started in February 2009, lasting until August 2009. When the noon-midnight meridian was crossed, the spacecraft was rotated 180 degrees around the nadir-zenith axis, to ensure that the solar panel remained illuminated at day.

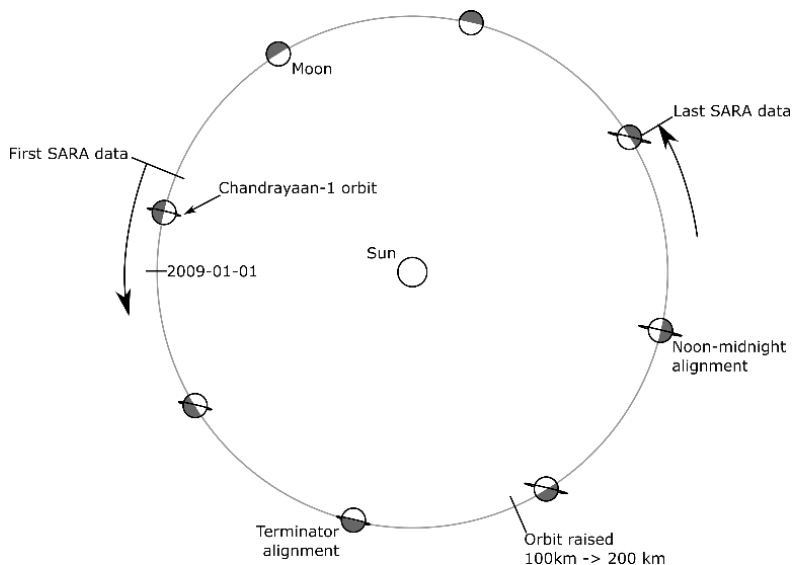


Figure 8 – Orbital configuration during the Chandrayaan-1 mission.

2.1.2 The SARA instrument

Although measuring particles rather than photon emissions from the surface, the SARA instrument [Barabash *et al.*, 2009] fits well in with the lunar surface-oriented mission. Surface emissions of particles can be diagnostic of surface properties, as well as space weathering processes. The scattered particles would also allow mapping of the solar wind precipitation onto the lunar surface, which e.g. could be compared with the surface maturity, to understand the role of the solar wind in space weathering [Futaana *et al.*, 2006].

SARA consisted of three components: a digital processing unit (DPU); the Solar Wind Monitor (SWIM), observing ions from space as well as the lunar surface; and the Chandrayaan-1 Energetic Neutrals Analyzer (CENA), observing ENAs from the lunar surface.

SWIM was included as a reference sensor for CENA's observations of the ENAs emitted from the lunar surface, and as a sensor of the lunar plasma environment. It was placed in a sideward-looking configuration (Figure 9), allowing its fan-like field-of-view to cover both space and surface directions. CENA also had a fan-like field-of-view, though centered at nadir. It was oriented with the fan-plane perpendicular to the spacecraft velocity vector (Figure 9), in order to maximize the surface area covered as the spacecraft moves in its orbit. SWIM and CENA are shown in Figure 10, and their performance characteristics are listed in Table 5.

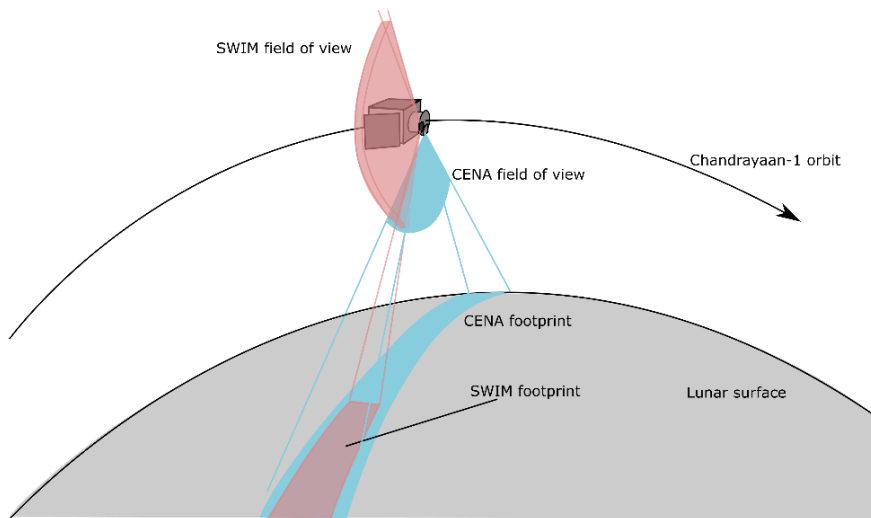


Figure 9 – Fields of view for SWIM and CENA relative to the lunar surface and orbit, and the sensor footprints (i.e. the surface area within the sensor field of view). Not to scale.

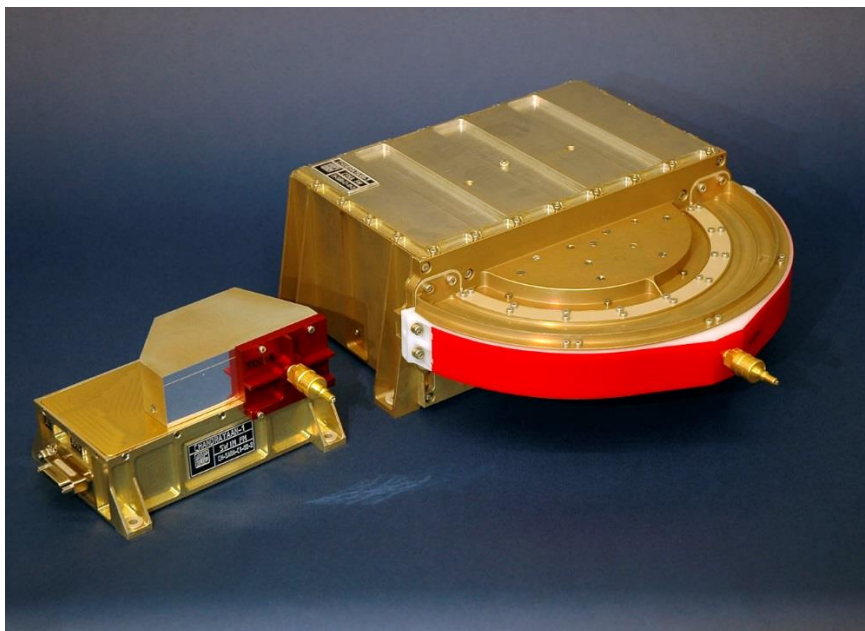


Figure 10 – The SWIM (left) and CENA (right) sensors. The red components covered the sensor apertures and were removed before flight. Photo credit: IRF.

Table 5 – Instrument performance of SWIM and CENA [Barabash *et al.*, 2009]. *The sensor could operate to 15 keV but was operated to 3 keV during the mission.

	SWIM	CENA
Field-of-view	9°x180°	15°x160°
Angular resolution	4.5°x22.5°	9°x25°
Energy range (per charge)	10 eV - 3 keV (15 keV*)	10 eV – 3.2 keV
Energy resolution ($\Delta E/E$)	7%	50%
Mass resolution	H ⁺ , He ⁺⁺ , He ⁺ , O ⁺⁺ , O ⁺ , >20 amu	H, O, (Na..Al), (K..Ca), Fe

2.1.3 The SWIM ion sensor

The design and working principles of SWIM is shown in Figure 11. The instrument allows ions to enter through a grid-covered aperture. Inside the grid, an electrostatic field is used to filter the ions based on their velocity vector. By only allowing a certain direction at a certain time, and then step-wise altering the electric field, the instrument can resolve and scan through different incidence directions. This initial section of the instrument is referred to as the deflection system.

Ions from the selected direction proceed to a section called the electrostatic analyzer (ESA). The ESA only allows ions of a certain energy (or rather, energy-per-charge) to pass to the next section. The ESA electric field is also swept-through to enable energy-resolved measurements over a wide energy range. Note that ions of higher energy-per-charge also require stronger electric fields in the deflection system for the direction selection. Thus, the two systems are coupled. In this way, the ESA not only determines the ion's energy-per-charge, but also greatly reduces the directional ambiguity from the deflection system.

Ions that pass through the deflection system are registered when they impact a START surface. Secondary electrons are emitted from the surface and detected by a channel-electron multiplier (CEM). The ions that impact the START surface are scattered towards a STOP surface, where they are also detected via secondary electrons. Thereby, the ions' time-of-flight (ToF) is measured, which gives their velocity (since the distance between the surfaces is known). Together with energy-per-charge information from the ESA, the measured velocity gives the particle mass-per-charge.

2.1.4 The CENA neutral atom sensor

CENA [Kazama *et al.*, 2006] measures ENAs. It allows these ENAs to enter the instrument through an aperture that almost forms a half circle (Figure 10, 12). In the first section (not shown in Figure 12), ions and electrons are rejected by an electric field, but the neutral ENAs pass through. Thereafter, the ENAs impact an

ionization surface that converts them into ions, so that their energies can be analysed by the next section, where these ions must travel along wave-like trajectories to pass. This is called the wave analyzer. Only ions with a certain energy is able to perform the required wave-like motion and pass to the next section. By changing the electric fields in the wave analyzer, different energies are selected. In the final section, the ions impact a START surface and their direction is determined by their impact position, via a secondary electron. The particle then continues on to the STOP surface, where its ToF is measured, which gives the particle velocity. The velocity and energy information are then combined to determine the particle mass.

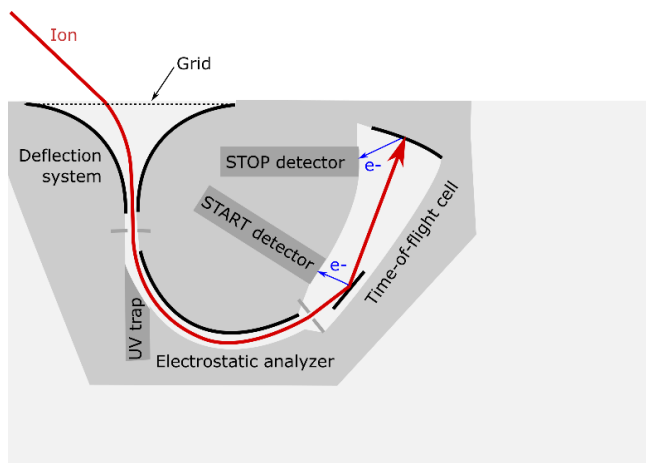


Figure 11 – Design of the Solar Wind Monitor (SWIM).

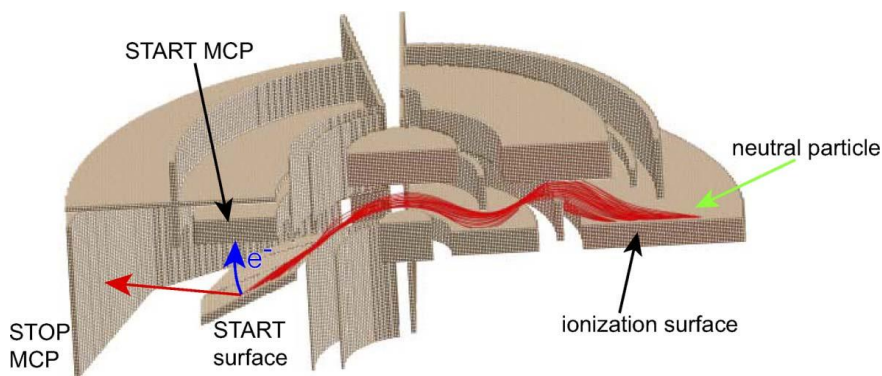


Figure 12 – Design of the Chandrayaan-1 Energetic Neutrals Analyzer (CENA). Reprinted from Kazama *et al.* [2006] with permission from Elsevier.

2.2 Upstream references

The upstream plasma parameters are essential data for putting observations at the Moon in context. SWIM contributes to this. In addition, we can utilize upstream spacecraft that are dedicated to solar wind measurements. For example, there are the Advanced Composition Explorer (ACE), the Wind spacecraft, and recently, the Deep Space Climate Observatory (DSCOVR). These are placed in the undisturbed solar wind upstream of the Earth-Moon system, orbiting the Sun-Earth L1 Lagrange point. As long as the Moon is in the undisturbed solar wind, these upstream measurements are good proxy-measurements for the ambient solar wind at the Moon. When comparing these data with lunar observations, the solar wind travel time of ~ 1 hour needs to be accounted for. In our studies that take place outside of the bow shock, we have used Wind data for this purpose. When the Moon is within the bow shock, the L1 measurements are not representative. Instead, we use Kaguya plasma measurements for comparison with SWIM and CENA observations.

2.2.1 *Wind plasma data*

Wind [Ogilvie and Desch, 1997] was launched in 1994 and flew by the Moon twice (where it also investigated the lunar wake, see Section 1.5.1) before it was inserted in a halo orbit (Figure 13) around the Sun-Earth L1 point. The data that we use are from the Solar Wind Plasma (SWE) instrument, and the Magnetic Field (MFI) instrument. The SWE data are available via the NASA National Space Science Data Center (NSSDC), the Space Physics Data Facility (SPDF), and the MIT Space Plasma Group (<http://web.mit.edu/space/www/>), courtesy of K. W. Ogilvie (NASA/GSFC), and A. J. Lazarus (MIT), and the MFI data are available via NSSDC and SPDF (<http://omniweb.gsfc.nasa.gov>), courtesy of A. Szabo (NASA/GSFC), and R. P. Lepping (NASA/GSFC).

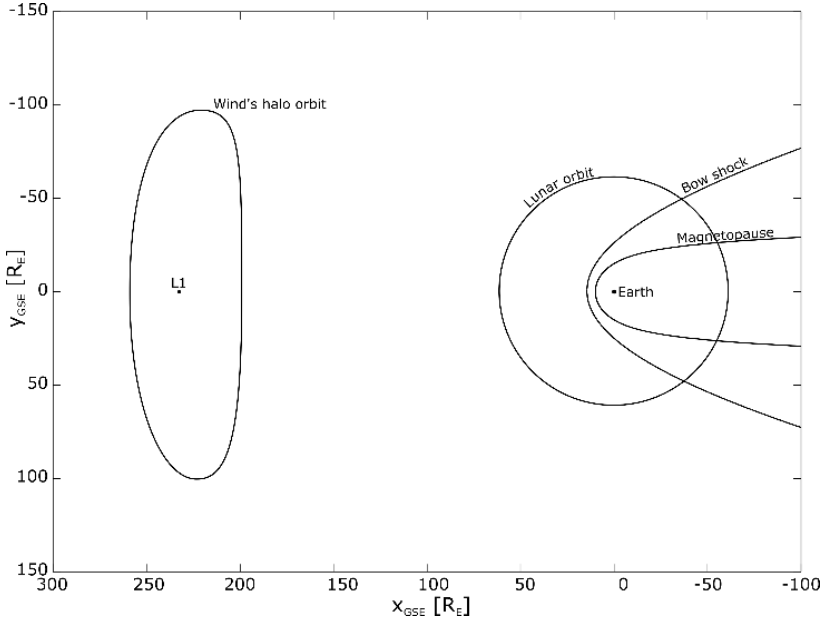


Figure 13 – The approximate orbits of the Wind spacecraft around the Earth-Sun L1 Lagrange point, and the Moon around the Earth. Typical locations for the terrestrial magnetopause and bow shock are also shown for reference. The coordinates are given in Earth radii (6371 km), in the Geocentric Solar Ecliptic coordinate system.

2.2.2 *Kaguya plasma data*

Kaguya (or Selenological and Engineering Explorer, SELENE) [Kato *et al.*, 2010] had a similar orbit as Chandrayaan-1, a polar orbit at a nominal altitude of 100 km. Its science objectives were to study the lunar surface and crust properties, interior structure, and lunar magnetism. It was brought down to lower altitudes toward the later part of the mission, allowing further study of the crustal fields and their interaction with the solar wind.

The mission was launched in 2007 and lasted until June 2009, and it was active for a large part of the Chandrayaan-1 mission. Thus, the observations from the two spacecraft (which had similar science goals) could favorably be used for joint studies.

In Paper V, where ENA scattering from the surface is analyzed, we use plasma data from the Ion Energy Analyzer (IEA) of the MAP-PACE plasma instrument [Saito *et al.*, 2010] on Kaguya.

2.3 Selenographical references

For the study of the solar wind-Moon interaction, it is also important to relate our particle observations with lunar surface properties and the lunar magnetic anomalies. In the thesis, the lunar albedo map from the Clementine spacecraft was used, as well as an empirical model of the crustal fields based on Lunar Prospector data.

2.3.1 *Clementine lunar albedo map*

The main topographical regions of the Moon are well distinguished by their visible light albedo. Thus, an albedo map is a simple but effective tool for providing topographical context. In addition, many selenographical landmarks are easily identifiable on such maps, aiding the read-out of location from the map.

Clementine (or the Deep Space Program Science Experiment, DSPSE) [Nozette *et al.*, 1994] was launched in 1994, targeted at mapping the Moon and a near-Earth asteroid (NEA), though its NEA transfer was aborted.

The lunar albedo map (Figure 14) was obtained by the High-Resolution Camera (HIRES) on Clementine, and is available from the U.S. Naval Research Laboratory (NRL) (<http://www.nrl.navy.mil/clementine/>).

2.3.2 *Lunar Prospector empirical crustal field model*

We have used an empirical crustal field model from Purucker [2008], and an updated version by Purucker and Nicholas [2010]. The model was developed based on Lunar Prospector magnetic field measurements. The map is shown in Figure 15. It can be accessed courtesy of M. E. Purucker and J. B. Nicholas from http://core2.gsfc.nasa.gov/research/purucker/moon_2010/index.html.

Lunar Prospector [Binder, 1998] studied the lunar surface composition, gravity field, and crustal magnetism. It is not trivial to measure the crustal magnetic field from orbital magnetic field measurements, because the decrease of the magnetic field with distance depends on the source depth, morphology, and coherence. Additionally, the solar and terrestrial magnetic fields dominate over crustal fields at orbital altitudes. Several global mapping studies have been performed. Hood *et al.* [2001] used Lunar Prospector magnetometer data, while Halekas *et al.* [2001] used Lunar Prospector electron data, deducing the magnetic fields from the properties of reflected electrons. Tsunakawa *et al.* [2010] has also made global maps of the magnetic anomalies, using Kaguya data.

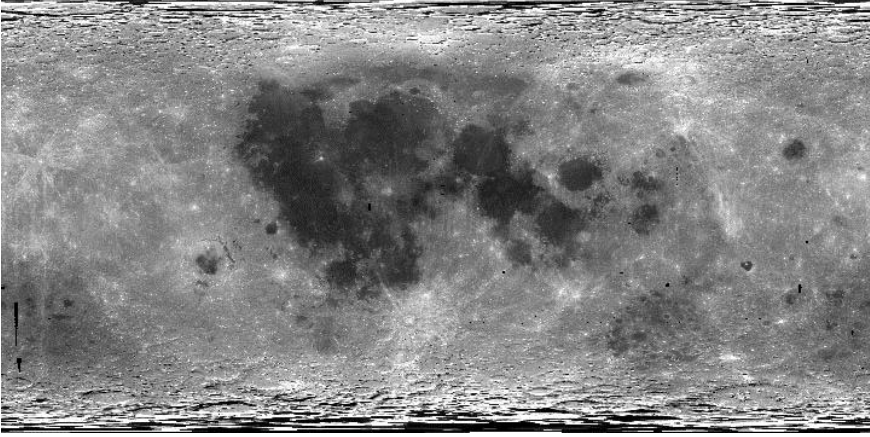


Figure 14 – Lunar albedo map from Clementine. Image credit: NRL.

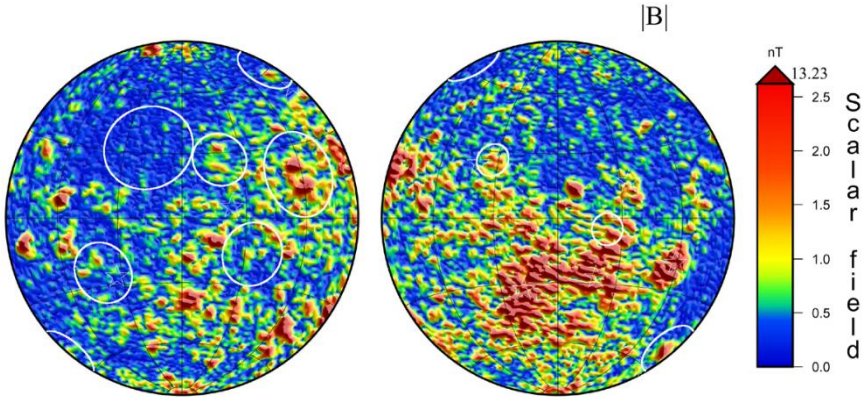


Figure 15 – Lunar crustal magnetic field strength at an altitude of 30 km, from an empirical model based on Lunar Prospector data, showing the near-side to the left and the far-side to the right. Reprinted from *Purucker and Nicholas* [2010] with permission from John Wiley and Sons.

2.4 Hybrid simulations

To investigate the complex three-dimensional and dynamic interaction on local scale between solar wind plasma and a lunar magnetic anomaly (Paper III), as well as on global scale where reflected protons interact with the upstream solar wind and modify the lunar plasma environment (Paper II), we employ modern computing tools, namely hybrid plasma solving software, executed on the Abisko computing cluster at the High Performance Computing Center North (HPC2N).

2.7.1 General principles

Hybrid models treat ions as particles and electrons as a fluid [e.g., *Holmström*, 2010]. Particle treatment is required to resolve kinetic phenomena below the scale of one particle gyroradius, as it tracks the motion of- and forces acting upon individual particles (though typically using fewer, macro particles, or a small set of particle moments to describe the distribution of a larger number of “real-world” particles). Magnetohydrodynamic (MHD) models, on the other hand, approximate both ions and electrons as fluids, and can use equations that describe their collective behavior without resolving individual particle motions. MHD models are computationally much more efficient, but do not resolve individual particle trajectories. Particle-in-cell (PIC) models treat both ions and electrons as particles. However, electrons that are treated as particles put orders-of-magnitude higher demands on the computer simulation than the ions do as the simulation needs to resolve spatial scales much smaller than the electron gyro-radius to track the motion. Their higher velocities similarly constrain the required time-resolution of the simulation.

In the lunar case, a reflected proton can have a gyro-radius on the order of 1000 km; comparable to the Moon itself. Thus, an MHD-simulation definitely cannot resolve proton dynamics on even a global lunar scale. Electrons, on the other hand, have gyro-radii on the order of 1 km, and can be treated with MHD simulations. Thus, hybrid simulations are used for global scale and meso scale lunar plasma simulations [c.f. *Kallio et al.*, 2012].

Even if global-scale lunar simulations do not need to resolve electron dynamics on 1 km scales, there is still a possibility that gyro-scale electron kinetics influence plasma dynamics on scales larger than that. If such effects are strong, then hybrid simulations may become inaccurate. This possibility is therefore discussed when comparing hybrid models with observations [e.g., *Holmström et al.* 2012; *Wang et al.*, 2010].

2.7.2 The FLASH hybrid code

The software used for the simulations is an open source software called FLASH, developed in collaboration with the DOE NNSA-ASC OASCR Flash Center at the University of Chicago. The hybrid solving versions used for our lunar simulations are presented by *Holmström* [2010]; *Holmström et al.*, [2012]. The implementations of the codes for our studies are discussed in more detail in Papers II and III, but here follows a brief overview of the code functionality.

The code uses macro particles to represent a large number of ions. Upon program initialization, the specific positions and velocities of the macro particles in the simulation grid are defined by random selection from a uniform spatial

distribution and a drifting Maxwellian velocity distribution. For each time-step of the simulation, the electric and magnetic field at the position of each ion is calculated, and then, the ion trajectory over the duration of one time-step is calculated. Ion trajectories are calculated from the Lorentz force, see Equation 3 in next section, and magnetic fields are updated using Faraday's law, Equation 8. The calculation of the electric field is where the hybrid assumptions are required. In the implementation presented by *Holmström et al.* [2012], the electric field is given by:

$$\mathbf{E} = 1/\rho_i(-\mathbf{J}_i \times \mathbf{B} + \mu_0^{-1} (\nabla \times \mathbf{B}) \times \mathbf{B} - \nabla p_e), \quad (1)$$

where \mathbf{E} is the electric field, \mathbf{B} is the magnetic field, \mathbf{J} is the current density, and μ_0 is the vacuum permeability (c.f. Section 3.1). i indicates ion terms and e indicates electron terms. ∇p_e is the electron pressure term. *Holmström* [2012] added a non-zero resistivity η to the model:

$$\mathbf{E} = 1/\rho_i(-\mathbf{J}_i \times \mathbf{B} + \mu_0^{-1} (\nabla \times \mathbf{B}) \times \mathbf{B} - \nabla p_e) + \eta \mu_0^{-1} (\nabla \times \mathbf{B}). \quad (2)$$

The simulation is then allowed to run until a quasi-steady-state solution for the plasma and fields is achieved. Simulation boundaries are periodic (grid cells at each edge of the three-dimensional simulation box are used to represent the plasma conditions in the non-existing grid cells just outside the opposite edge), to avoid edge effects. This means that the simulation box must be large enough so that a steady-state is achieved before the Moon interacts with itself through the simulation boundaries.

3. Proton interactions with lunar magnetic anomalies

In this chapter, we introduce the physics of particle interactions with magnetic fields, and present Moon-related results. Then, we discuss the effects of the proton reflection on the lunar environment.

3.1 Plasma interactions with magnetic fields

The electrodynamic interaction between charged particles and electromagnetic fields is essential to plasma physics. In this section, we briefly describe a few relevant electrodynamic equations.

3.1.1 *Fundamental laws of electrodynamics*

The force that an electric field applies to a charged particle is given by $\mathbf{F}_E = q\mathbf{E}$, where q is the particle charge and \mathbf{E} is the electric field. The force applied by a magnetic field \mathbf{B} to a particle depends on the particle velocity \mathbf{v} as $\mathbf{F}_B = q\mathbf{v} \times \mathbf{B}$. The total force, called the Lorentz force is thus:

$$\mathbf{F} = q(\mathbf{E} + \mathbf{v} \times \mathbf{B}). \quad (3)$$

This equation can be used to solve the motions of individual particles, given that the force fields are known. Example trajectories are shown in Figure 16. The particle travels in a cycloid trajectory, with a specific cyclotron radius or gyro-radius (also called Larmor radius), given by:

$$r_c = mv_{\perp}/(|q|B), \quad (4)$$

where v_{\perp} is the component of the particle velocity that is perpendicular to the magnetic field.

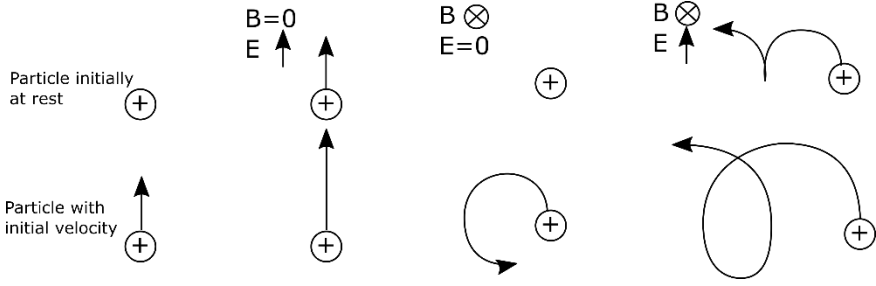


Figure 16 – Ion trajectories in constant external electric and magnetic fields.

However, when a particle responds to the fields, it also modifies the fields in return. The situation becomes complicated when there are several particles to account for, if each of which significantly modifies the force fields that act upon the other particles. The situation can be described by Maxwell's equations, a system of differential equations describing the relationships between the force fields \mathbf{E} and \mathbf{B} and the particle distributions:

Gauss' law describes the electric field created by an accumulation of charges:

$$\nabla \cdot \mathbf{E} = \rho / \epsilon_0, \quad (5)$$

Where ρ is the charge density and ϵ_0 is the vacuum permittivity.

There is, as far as we know, no equivalent to an electric charge for magnetism (no magnetic monopoles). Thus, Gauss' law for magnetism is:

$$\nabla \cdot \mathbf{B} = 0. \quad (6)$$

Instead, magnetic fields arise from currents, and time-varying electric fields, as expressed by Ampere's law:

$$\nabla \times \mathbf{B} = \mu_0 (\mathbf{j} + \epsilon_0 \partial \mathbf{E} / \partial t), \quad (7)$$

Where μ_0 is the vacuum permeability.

Additionally, a time-varying magnetic field is related to the curl of the electric field as expressed by Faraday's law:

$$\partial \mathbf{B} / \partial t = -\nabla \times \mathbf{E}. \quad (8)$$

3.1.2 Boundaries and pressure balance

There are several different approaches to solving the above equation system, using various approximations and assumptions, e.g., numerical hybrid solvers (Section 2.4). However, one can also take advantage of concepts such as energy-

and momentum conservation or, for systems in steady-state, the balance of currents and of forces. A typical example is the calculation of a planetary magnetopause distance based on the distance from a magnetic dipole where the magnetic pressure balances the solar wind pressure.

The solar wind pressure on a magnetic barrier is divided into dynamic pressure p_{dyn} , thermal pressure p_T , and magnetic pressure p_B :

$$p_{\text{dyn}} = \sum_i n_i m_i v_{bi}^2 \cos(\alpha) \approx n_p m_p v_{sw}^2 \cos(\alpha), \quad (9)$$

where n_i , m_i , and v_{bi} are the number density, mass density, and bulk velocity of particle species i , α is the bulk incidence angle onto the barrier, the bulk velocity v_{sw} is approximately the same for each species, and the dynamic pressure from protons ($i=p$) dominates;

$$p_T = \sum_i n_i k_B T_i \approx 2n_p k_B T_{sw}, \quad (10)$$

where k_B is the Boltzmann constant, the total electron and ion density is approximately $2n_p$, and T_{sw} is roughly constant between the species;

$$p_B = B_{IMF}^2 / 2\mu_0, \quad (11)$$

where B_{IMF} is the solar wind magnetic field (the IMF).

The upstream/external pressures are balanced by the sum of the pressures from the other side of the barrier. In the case of the sub-solar impact of the solar wind with a magnetosphere, the solar wind pressure is dominated by p_{dyn} , and the magnetospheric pressure is dominated by $p_{B_MS} = B_{MS}^2 / 2\mu_0$, where the planetary magnetic field B_{MS} decreases with distance r from the planet. Thus, the subsolar magnetopause of a magnetized planet exists where

$$n_p m_p v_{sw}^2 = B_{MS}(r)^2 / 2\mu_0. \quad (12)$$

A different example exists in the lunar tail, where the refilling plasma is stopped by the compressed magnetic field in the wake of the Moon [*c.f. Holmström et al., 2012*]. In that situation, the external plasma pressure rather than the dynamic pressure is being balanced by the magnetic pressure.

3.2 Proton dynamics at crustal magnetic anomalies

From pressure-balance calculations, it is possible to estimate the maximum stand-off distance of the solar wind over a magnetic anomaly (with known magnetic field configuration). However, this doesn't mean that such a boundary necessarily can form. If the incoming particles have gyro-radii comparable to the scale of the magnetic obstacle, they may not manage to turn around before they

have flown past the obstacle, or e.g. impacted the planetary surface above the source of the magnetic field. In such a case, no magnetopause forms.

3.2.1 *Mini-magnetospheres and sub-magnetospheric interactions*

The formation of a magnetosphere by magnetic fields of scale sizes comparable to the proton gyroradius (here referred to as mini-magnetospheres), and sub-magnetospheric interactions (in which a magnetosphere does not fully form) were discussed by *Greenstadt* [1971a,b], when considering the solar wind interaction with magnetized asteroids. They presented three conditions required for the formation of a mini-magnetosphere that successfully stands-off the solar wind: (1) The magnetic field must be strong enough from a pressure-balance point-of-view (see above). (2) The magnetopause distance from the surface must be greater than the solar wind stopping distance, i.e., the vertical distance required to turn-around the solar wind plasma. (3) The lateral (horizontal) scale size of the magnetic obstacle must be large enough to exclude edge-effects.

If these criteria are not met, the solar wind will fill-in the crustal field and be deflected but not creating a proper void. Nevertheless, such an interaction would create various electromagnetic noise [*Greenstadt*, 1971a,b and references therein]. If the solar wind deceleration is large enough, a magnetosonic shock would form even without a void region. Whistler waves would also arise from the disturbance of the solar wind, possibly creating a standing whistler wave [*Greenstadt*, 1971a].

The lunar case has been addressed by analytical approaches [e.g., *Borisov and Mall*, 2003; *Sadovski and Skalsky*, 2014], MHD simulations [e.g., *Harnett and Winglee*, 2000, 2002, 2003a], kinetic simulations [*Zimmerman et al.*, 2015], hybrid simulations [e.g., *Kallio et al.*, 2012; *Fatemi et al.*, 2015a], PIC simulations [e.g., *Poppe et al.*, 2012; *Deca et al.*, 2014], laboratory studies [e.g., *Wang et al.*, 2012; *Blewett et al.*, 2012; *Shaikhislamov et al.*, 2014], as well as studies at the Moon [e.g. *Clay et al.*, 1975; *Lin et al.*, 1998; *Halekas et al.*, 2006; 2008; 2010; *Saito et al.*, 2012; *Wieser et al.*, 2010; *Lue et al.*, 2011; *Vorbuerger et al.*, 2012; *Futaana et al.*, 2013]. The majority of the work on the topic finds a sub-magnetospheric type of interaction appears most plausible, for most of the lunar magnetic anomalies, most of the time.

However, in some situations, or perhaps commonly but on small scales, voids may form. Lunar albedo swirls (bright features on the lunar surface at strong magnetic anomalies) may be indicative of small plasma voids, where surface weathering is reduced [e.g., *Garrick-Bethell et al.*, 2011; *Kramer et al.*, 2011a,b]. These regions are small (~10s km) and are yet to be directly sampled by plasma instruments or sufficiently resolved from ENA remote-sensing (c.f. Section 4.3).

3.2.2 Proton deceleration and deflection

Clear evidence of deceleration and deflection of the solar wind near magnetic anomalies were observed by the Apollo missions [Clay *et al.*, 1975]. A larger picture was enabled by ENA-remote sensing, allowing imaging of the plasma precipitation by the characteristics of the scattered ENAs (Figure 17). Wieser *et al.* [2010] presented the first ENA image of a lunar magnetic anomaly, showing a clear enhancement around the crustal field and a decrease in the center. The decrease was $\sim 20\%$, thus not a complete void, but there could be voids present that are smaller than the ENA image resolution.

Wieser *et al.* [2010] also observed a reduction in the ENA energy where the ENA flux was reduced. Vorburget *et al.* [2013] applied ENA imaging to the majority of the lunar surface, clearly observing reduction and deceleration of the solar wind at magnetic anomalies. The deceleration was also observed by orbital plasma instruments [Saito *et al.*, 2012]. Futaana *et al.* [2013] implemented a technique for measuring the surface potential using the observed ENA energy. These studies suggest surface potentials of ~ 200 V, which help to deflect the protons of the solar wind from the surface.

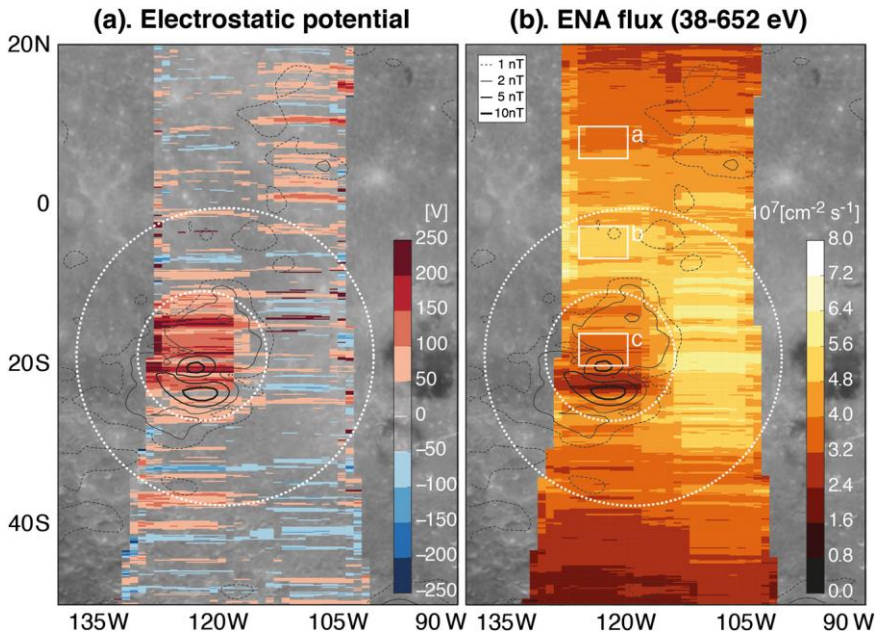


Figure 17 – The inferred surface potential at magnetic anomaly (a) and the precipitating flux of solar wind protons (b), as observed in backscattered ENA flux. Reprinted from Futaana *et al.* [2013] with permission from John Wiley and Sons.

3.2.3 *Proton heating and reflection*

The solar wind protons are not only deflected into the nearby regions, but some are also deflected/reflected away from the Moon [Saito *et al.*, 2010; Lue *et al.*, 2011]. The reflected proton streams were observed to have temperatures of 100s eV, compared to the ~10 eV of the solar wind). Reflection rates were 10%-50% or higher at the strongest magnetic anomalies. Saito *et al.* [2012] reported that the heating appears to occur at lower altitudes than the deceleration. We discuss the topic further in Paper I.

3.3 Implications of the solar wind interaction with lunar magnetic anomalies

The solar wind interaction with lunar magnetic anomalies has implications not only for the plasma physics involved, but also for the lunar plasma environment on local and global scales, and the surface evolution at magnetized surface areas.

3.3.1 *Effects on the local environment*

The lunar plasma environment is locally modified by the presence of a magnetic anomaly. The plasma is heated and decelerated, and the precipitation pattern is changed. The electric fields set up by the interaction charges the surface up to 100s V positive [e.g., Futaana *et al.*, 2013; Fatemi *et al.*, 2015a], where it would otherwise be ~5 eV in sunlight or 100s V negative in shadow. This can affect the dust environment. Positively charged dust grains from surrounding regions may lift to higher altitudes or deflect away from the area, while negative dust grains, lofted from the lunar nightside may sink towards the positively charged surface at the anomaly [Garrick-Bethell *et al.*, 2011]. On the other hand, local plasma wakes from e.g., craters, hills, and other objects may be more easily refilled by the hotter plasma, and strong electric fields created at local shadows may be more dispersed in these conditions [Farrell *et al.*, 2010].

3.3.2 *Effects on the local surface evolution*

The decrease of precipitating solar wind fluxes and energies slows the aging of the lunar surface due to solar wind weathering. In addition, the implantation of volatiles and water-forming protons is reduced, as supported by Chandrayaan-1 M³ observations [Kramer *et al.*, 2011a, b] of weaker hydroxyl signatures from albedo swirls at magnetic anomalies. Albedo swirls also have dark lanes, with more hydroxyl, suggesting enhanced precipitation at these regions. (Albedo swirls are visibly brighter regions near magnetic anomalies that are uncorrelated to other topographic features.)

The reduced solar wind weathering allows us to separate micro-meteorite and solar wind-induced weathering, including the effects of different solar wind species, differently well shielded.

The effects of magnetic anomalies on dust movement could also cause surface evolution as fine-grained dust accumulates at certain regions over time, providing an alternative explanation to albedo swirls [Garrick-Bethell *et al.*, 2011].

3.3.3 Effects on the global environment

Protons that are reflected from magnetic anomalies can reach far upstream and downstream and even significantly disturb the solar wind flow [e.g., Fatemi *et al.*, 2014; Halekas *et al.*, 2012] (Figure 18), as discussed further in Paper II. This changes the global solar wind precipitation, increasing plasma to the lunar nightside as well as causing fore-shock like higher energy proton impacts on the lunar dayside. Nishino *et al.* [2009] pointed out that in this (“Type-II”) type of plasma entry into the wake, the protons lead and the electrons follow, contrary to the classical (“Type-I”) wake refilling where electrons lead and protons follow. Thus, the charge-separation electric fields involved in this deep-wake entry are oppositely oriented compared to the Type-I wake refilling. This may even charge the deep-wake lunar surface positive rather than the nominal negative potentials [c.f. e.g. Halekas *et al.*, 2011].

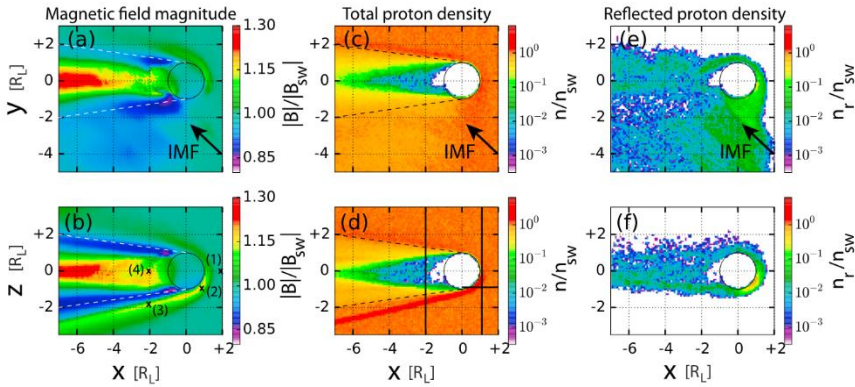


Figure 18 – Global effects of solar wind reflection from magnetic anomalies. Reprinted from Fatemi *et al.* [2014] (Paper II) with permission from John Wiley and Sons.

4. Proton interactions with lunar regolith

Proton interactions with lunar regolith follow very different rules than the interactions with magnetic anomalies. Here, we review basics of particle-surface interactions, with focus on topics relevant for proton interaction with regolith. We then briefly review recent observations and discuss implications of proton scattering from the Moon.

4.1 Particle-surface interactions

Particle-surface interactions is an important field for both surface science and space physics. The interactions are important for surface evolution, surface diagnostics, surface charging, and near-surface environments. In this section, we will overview the main interaction mechanisms, with a focus on themes relevant for \sim keV ion and ENA scattering from surfaces.

4.1.1 Basic concepts

When a low-energy (\sim keV) ion impacts a surface, it can knock-off surface atoms. This is called sputtering, and is often used for surface composition analysis [*e.g.*, Johnson and Baragiola, 1991]. The incident ion may also be reflected, i.e., scattered from the surface. Scattering is also used to study surface properties indirectly [*e.g.*, Niehus *et al.*, 1993]. The ion may also be absorbed and implanted into the surface. The ion impact with the surface can also affect the charge of the surface in several ways. Electrons may be emitted from the surface, charging the surface positively. Sputtered particles may be neutral, positive, or negative, and the same applies to scattered ions, which can change their charge state during the scattering process. The surface and particles may also reach excited states as a result of the interaction, and photon emissions can also be involved. An overview of particle-surface interactions is shown in Figure 19.

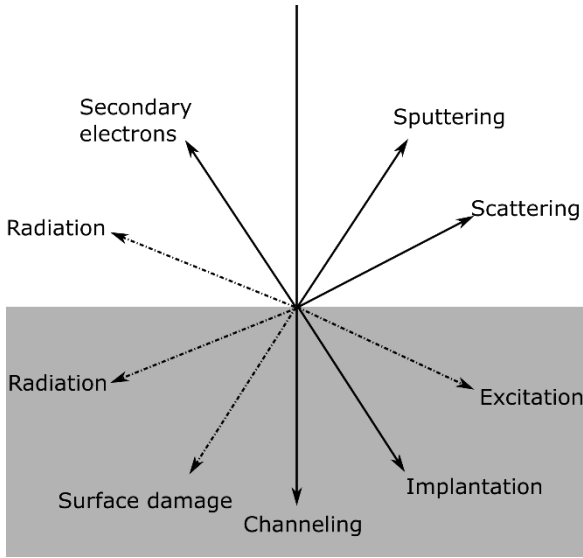


Figure 19 – Particle-surface interactions. Adapted from Lucas [1973].

4.1.2 Collisions and particle movement in a solid material

A particle can travel within a solid surface material with a certain energy-dependent path length between collisions, and may experience one or more collisions until it escapes the material or comes to rest. The energy loss per distance in the surface is called stopping power. The collisions experienced by the particle can be atomic or electronic, and elastic or inelastic. This determines the energy loss per collision.

Particle collisions with surface atoms at energies >100 eV are fast enough to be considered as two-body problems, and are commonly evaluated as elastic collisions between two hard spheres [e.g., Niehus *et al.*, 1993]. The energy loss in such a collision depends on whether it's a head-on or tangential collision. The ratio of the remaining energy E_1 to the initial energy E_0 is:

$$(A-1)/(A+1) < E_1/E_0 < (A-1)^2/(A+1)^2, \quad (13)$$

where $A = m_s/m_p$ is the ratio between the mass of the surface atom m_s and the mass of the fast particle m_p . Thus, in this type of collision, the energy loss is proportional to the particle energy.

At higher energies, instead of elastically interacting with a target atom, the ion may interact directly with an electron, which may absorb some of the energy by reaching a higher energy state, causing an inelastic collision. On metals, with a conduction band of free electrons, the interaction can be described as a collision

between the ion and the electron. On the other hand, for insulators, the electronic stopping is more likely the case of electron capture, i.e., charge-exchange, where energy loss occurs if the electron absorbs some of the kinetic energy of the ion. The electron can then be lost in further collisions, or an additional electron can be added, forming a negative ion. Several charge-exchange cycles may successively drain energy from the particle. Electronic stopping is typically characterized by a proportionality between the energy loss and the particle speed. The threshold for the onset of electronic stopping has been found for protons to be ~ 50 eV (100 km/s) on Si; and ~ 2.5 keV (700 km/s) on Al_2O_3 and SiO_2 . [e.g., *Draxler et al.*, 2005 and references therein].

4.1.3 Charge-exchange processes

One way for an ion to capture an electron is resonant neutralization. Resonant neutralization requires that there is an overlap between the energies of electrons at the surface and the atomic energy level that an electron could be captured into. At metal surfaces, there is a wide conduction band of available electron energies. For non-metals, the interaction must be with an electron bound to a molecule or atom. These energies are typically not identical to the resonant energy. Nevertheless, a small amount of kinetic energy can be transferred from the ion to the electron to enable resonant capture. Another mechanism available to both metals and non-metals is Auger neutralization. In this process, a surface electron transfers energy to another surface electron (which may be excited or released from the surface) so that the former electron achieves the specific energy level for capture. [e.g., *Massey*, 1950; *Niehus et al.*, 1993]

Because electrons are much more mobile than ions, charge-exchange processes occur quickly compared to the ion-surface interaction time. This means that a particle traveling through the surface quickly reaches an equilibrium charge state. As supported by experimental observations, this suggests that the initial charge of the incident particle is of little consequence for its final charge [e.g., *Verbeek et al.*, 1976; *Eckstein*, 1981], especially if the particle stays at the surface longer than the time scale of one collision. Nevertheless, a clear dependence between particle impact speed and exit charge state is observed [e.g., *Massey and Burhop*, 1952]. This is likely an indication of how the final charge state is determined when the particle leaves the surface, and is rather a function of the particle exit velocity [e.g., *Eckstein*, 1981]. The exit direction has also been seen to influence the charge state. *Eckstein* [1981] presented the positive charge fraction as a function of the perpendicular (to the surface) exit velocity (v_{perp}):

$$\eta^+ \propto \exp(-v_c/v_{\text{perp}}), \quad (14)$$

where η^+ is the ion reflection efficiency and v_c is a constant that is specific for a certain particle-surface combination. It has been found that the charge fraction also depends on the incidence angle. This may be explained by the different amount of energy loss resulting from different incidence angles on a flat surface [e.g., *Massey and Burhop*, 1952, and references therein]. Grazing-angle scattering on a flat surface is a special case, which is common in applications, where the incident ion does not enter the bulk of the surface material, but scatters superficially, with lesser dispersion of energies and exit directions [e.g., *Niehus et al.*, 1993].

The charge fraction also depends on the amount of energy required to release an electron from the surface, i.e. the surface work function. *Massey and Burhop* [1952, and references therein] expressed the ion reflection probability as:

$$\eta^+ \propto \exp((\phi - I)/k_B T), \quad (15)$$

where ϕ is the work function, I is the ionization energy, k_B is the Boltzmann constant, and T is the surface temperature.

4.2 Proton scattering from regolith

Scattering of solar wind protons may take the form of scattered hydrogen ENAs, protons, or even negative hydrogen ions. Here, we describe some of the predicted and observed properties of the lunar surface scattering of the solar wind.

4.2.1 Charge states

Wekhof [1981] discussed solar wind scattering from the Moon, using results from proton scattering from ThO_2 [*Behrisch et al.*, 1975; *Verbeek et al.*, 1976]. ThO_2 (with a work function $\phi = 2$ eV) has similar properties as SiO_2 , the most abundant compound in regolith, ($\phi = 3$ eV [*Sidorov et al.*, 2011]). *Wekhof* [1981] suggested that ~5% and ~10% of the scattered particles should be positively and negatively charged, respectively. For a target with slightly higher work function, *Wieser et al.* [2003] studied solar wind-energy proton scattering from MgO_2 ($\phi = 5$ eV [*Giordano et al.*, 2003]). *Wieser et al.* [2003] found charge fractions in the scattered beam of ~7% positively and ~4% negatively charged for incident protons of ~1 keV. However, it should be noted that they used grazing-angle scattering and thus, for higher incidence angles, the energy loss may be higher- and charge fractions lower than the reported values.

The recent studies that confirmed solar wind scattering from the Moon also found that the scattered particles were mostly hydrogen [*McComas et al.*, 2009; *Wieser et al.*, 2009], with a proton component [*Saito et al.*, 2008] of <10% of the

scattered neutral particles. The presence of a negative component remains unknown.

4.2.2 Scattering rate

The total scattering rate suggested by *Wekhof* [1981] and *Starukhina* [2003] was $\sim 20\%$ of the solar wind. However, a large difference between laboratory surfaces and the lunar surface is the roughness, which may increase the absorption. Nevertheless, the recent studies found remarkably high scattering rates (10%-20% hydrogen [*McComas et al.*, 2009; *Wieser et al.*, 2009]; 0.1%-1% protons [*Saito et al.*, 2008], indeed similar to the suggestions by *Wekhof* [1981].

4.2.3 Scattering function

The roughness clearly had an effect on the scattering function though. *Schaufelberger et al.* [2011] studied the directional scattering function for hydrogen ENAs from the lunar regolith, finding that it was very diffuse at normal incidence, while strongly retro-reflecting at shallower angles, with a smaller forward-scattering component. The retro-reflection suggests an opposition effect, similar to that of photon reflection from the Moon, which is due to the surface micro-structure. Figure 20 shows the scattering function of solar wind off regolith.

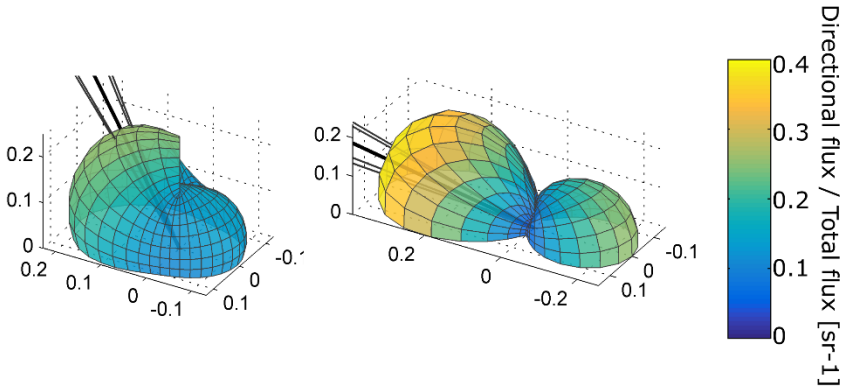


Figure 20 – Solar wind scattering function as hydrogen ENAs from the lunar regolith. Adapted from *Lue et al.* [2015a], using a model by *Vorburger et al.* [2013]. Black lines represent the incident solar wind direction, and the colored surfaces indicate the scattering function.

4.2.4 Energy spectrum

Similarly, the regolith structure caused a clear difference in energy loss, compared to laboratory results. Although a large amount of the solar wind makes it out from the surface, most of the particles experience many collisions in the

surface material. Hence, the ENA energy spectrum has a peak around zero exit energy, and an approximately Maxwellian distribution [Futaana *et al.*, 2012]. On the other hand, likely due to the velocity dependent charge-exchange, the proton component has a peak at a higher energy [Lue *et al.*, 2014] (Paper IV). The empirically modeled spectra are shown in Figure 21.

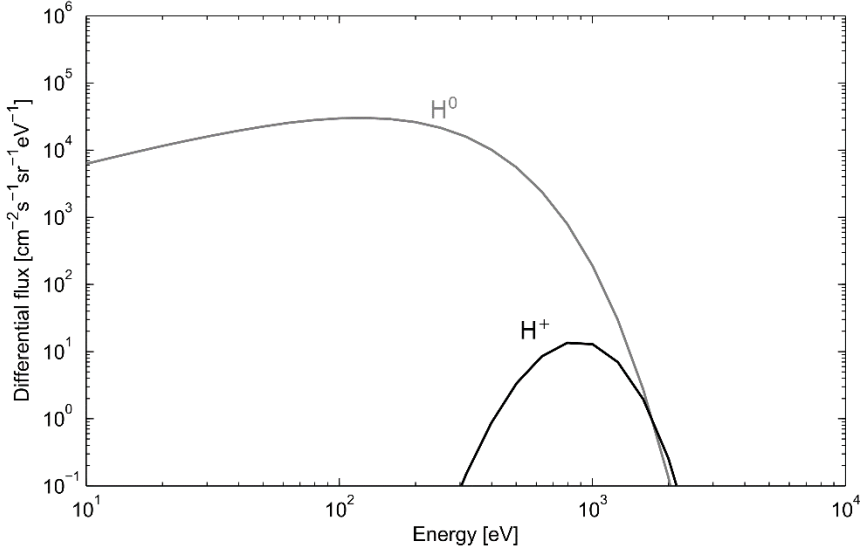


Figure 21 – Energy spectra of scattered hydrogen and protons from the lunar regolith, for a 450 km/s solar wind speed, and solar wind density: 5 cm⁻³, based on models from Futaana *et al.* [2012] and Lue *et al.* [2014], respectively.

4.3 Implications of the solar wind interaction with regolith

Like proton reflection from magnetic anomalies, reflection from regolith affects local and global environments, and the global exchange of material between the surface and the lunar exosphere and space. Additionally, the scattered particles are highly useful for remote-sensing applications.

4.3.1 Effects on the plasma environment

The scattering process can enhance solar wind access into otherwise protected areas such as craters and caves, e.g., by scattering from nearby walls.

Globally, the scattered protons have a similar behavior (Figure 22) as the magnetically reflected protons (Section 3.3.3), although more diffuse and less likely to induce shock-like disturbances of the solar wind. They also have a different relationship with the solar wind parameters. While the magnetic anomalies become suppressed by increasing solar wind pressure [Vorburger *et al.*, 2012], the scattering rate for protons increases exponentially with the solar

wind speed [Lue *et al.*, 2014]. Thus, the global lunar interaction may fluctuate between a magnetic anomaly-dominated and a surface-dominated interaction, providing excellent opportunities for comparative planet-solar wind interaction studies.

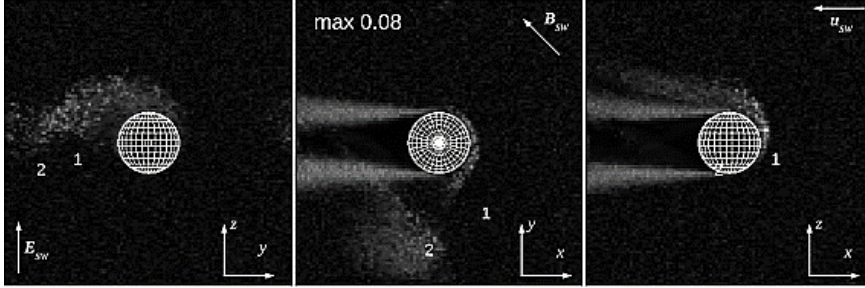


Figure 22 – Global distributions of surface-reflected protons in the lunar plasma environment. The figure shows the non-solar wind velocity component of the proton flux and therefore shows not only reflected protons but also wake-refilling solar wind. Reprinted from Holmström *et al.* [2011] with permission from John Wiley and Sons.

4.3.2 Effects on the volatiles budget

With the exception of argon, the main components of the lunar exosphere are a result of the solar wind-Moon interaction. The exospheric Ne, He, and H₂, escaping from the lunar soil, are mainly of solar wind origin, and fluctuate in correlation with solar wind changes [Benna *et al.*, 2015], as predicted by Hinton and Taesch [1964]. Solar wind scattering and sputtering phenomena act to reduce the amount of volatiles implanted in the lunar soil, thus also reducing the source of the exosphere (the scattered and sputtered ENAs do not contribute to the exosphere since they escape the lunar environment within seconds). Hodges [2011] suggested that hydrogen ENA scattering could explain the lower than predicted exospheric H₂ density, assuming that the majority of the solar wind leaves the lunar surface energetic enough to not remain as exosphere.

4.3.3 Remote-sensing applications

Observing and understanding scattered particles has provided us with a method to remote-sense properties of precipitating plasma and electric conditions at the surface [e.g., Futaana *et al.*, 2006; 2013; Wieser *et al.*, 2010; Vorburger *et al.*, 2012; 2013; 2015]. Further understanding and more detailed observations of both scattered and sputtered particles can enable remote-sensing also of surface structure and composition.

5. Summary of papers

Paper I

Strong influence of lunar crustal fields on the solar wind flow

Lue et al. [2011], Geophysical Research Letters

Our studies of the proton interaction with lunar magnetic anomalies begin with a characterization and mapping of the reflected proton streams from these magnetic anomalies. The reflected protons have bulk energies near the solar wind energy but are significantly heated, and their flow directions are mainly from the horizon, clearly separated from the solar wind protons in the chosen orbit geometry. The fluxes were clearly correlated to the locations of magnetic anomalies, and we estimate that up to ~50% of more of the solar wind is reflected at the most effective magnetic anomalies; ~10% as an average number over the observed magnetic anomalies.

This paper is based on work performed for my Master's thesis [Lue, 2011] and I did the data analysis, production of figures, and most of the writing. Dr. Yoshifumi Futaana instructed me in the use of SARA data and introduced me to the scientific background.

Paper II

Effects of protons reflected by lunar crustal magnetic fields on the global lunar plasma environment

Fatemi et al. [2014], Journal of Geophysical Research: Space Physics

We followed up on the implications of Paper I by investigating, with hybrid simulations, the global influence that the observed proton streams have on the lunar plasma environment. The results show that the reflected protons reach the near-Moon wake, which is otherwise inaccessible to the solar wind, and that the reflected protons that are sent into the solar wind create significant disturbances to the solar wind flow. The simulation results therefore provide a plausible explanation for previous observations of these effects.

My role in this work led by Shahab Fatemi was to analyze Chandrayaan-1 data of proton reflection directions and provide reference data so that we could develop a function for the directional distributions of reflected protons that was consistent with the observations. I also provided the proton reflection rate map developed in Paper I, which was used as an input in the computer simulations, and shown in Figure 1 of the paper.

Paper III

Solar wind plasma interaction with Gerasimovich lunar magnetic anomaly

Fatemi et al. [2015a], Journal of Geophysical Research: Space Physics

We investigate the local-scale plasma properties and dynamics of the solar wind interaction with a specific magnetic anomaly at the crater Gerasimovich. We present small-scale structures forming in the magnetic anomaly, and the plasma properties in these, as well as the variability of the interaction as a function of incident plasma properties, showing a smoother, deflection-dominated interaction at low solar wind pressures, and a more chaotic interaction at higher solar wind pressures, when the magnetic field is still capable of holding off a large fraction of the solar wind, but the interaction region is compressed to a smaller area.

The majority of this work was performed by Shahab Fatemi. I reviewed the Chandrayaan-1 data coverage over Gerasimovich and provided reference times of interest for the comparison of simulation results and observations. I also participated in the discussion and interpretation of the results.

Paper IV

Chandrayaan-1 observations of backscattered solar wind protons from the lunar regolith: Dependence on the solar wind speed

Lue et al. [2014], Journal of Geophysical Research: Planets

In this paper, we characterize the protons scattered from the lunar regolith, and relate their properties to those of the incident solar wind, with a focus on the dependence on the speed of the incident protons. We find that the fraction of scattered proton flux to the incident solar wind flux varies by at least two orders of magnitude (0.01%-1%) for solar wind speeds of 250-550 km/s. We also investigate the energy spectrum of the scattered protons. By comparing these results to known characteristics of scattered hydrogen atoms, we suggest that both effects are consistent with the charge-state being a function of the particle exit speed from the surface.

I identified and proposed an explanation for the trend, performed the statistical analysis, produced the figures and wrote the majority of the text.

Paper V

Scattering characteristics and imaging of energetic neutral atoms from the Moon in the terrestrial magnetosheath

Lue et al. [2015a], under revision for Journal of Geophysical Research: Space Physics.

Here, we investigate the effect of the incident proton temperature on the scattering characteristics. We modify existing scattering models to account for the proton temperature. We then validate the results by studying ENA scattering from the Moon in the magnetosheath. The resulting ENA images also show shielding of the surface by lunar magnetic anomalies, showing drastically different results at low solar-zenith angles compared to high solar-zenith angles. We see no effects of mare/highland differences.

I performed most of the data analysis and the model adaptations, and produced the figures and most of the text. The study required the use of data from the Kaguya lunar orbiter, and it became a joint effort between the Chandrayaan-1 and Kaguya teams. Dr. Yoshifumi Futaana had a major role in proposing and setting up the study. I was instructed and supported in the use of data from MAP-PACE (on Kaguya) by Prof. Yoshifumi Saito and Dr. Masaki Nishino.

Paper VI

Solar wind scattering from the surface of Mercury: Lessons from the Moon

Lue et al. [2015b], in preparation.

In this paper, which is in preparation, we apply the lessons learned at the Moon to discuss implications for Mercury, where similar solar wind-regolith interactions may take place. We review the current view of the plasma environments at Mercury and the Moon, and the solar wind scattering process as observed at the Moon, and then use the lunar scattering models with modeled Hermean plasma parameters to simulate solar wind scattering at Mercury.

I have done the data analysis, model implementations, figures and most of the text for this paper. Dr. Yoshifumi Futaana has also made significant contributions to the text. The initial concept of the study was proposed by Dr. Martin Wieser and Prof. Stas Barabash, and they identified an interesting event at the Moon.

References

- Alfvén, H. (1957), On the theory of comet tails, *Tellus* 9:92-6, doi:10.1111/j.2153-3490.1957.tb01855.x.
- Asbridge, J. R, S. J. Bame, and I. B. Strong (1968), Outward flow of protons from the Earth's bow shock, *J. Geophys. Res. Space Physics*, 73, 17, 5777-5782, doi:10.1029/JA073i017p05777.
- Bame, S. J., A. J. Hundhausen, J. R. Asbridge, and I. B. Strong (1968), Solar wind ion composition, *Phys. Rev. Lett.*, 20, 393, doi:10.1103/PhysRevLett.20.393.
- Barabash, S., et al. (2009), Investigation of the solar wind-Moon interaction onboard Chandrayaan-1 mission with the SARA experiment, *Curr. Sci.*, 96, 4, 526-532.
- Barnes, A., P. Cassen, J. D. Mihalov, and A. Eviatar (1971), Permanent lunar surface magnetism and its deflection of the solar wind, *Science*, 172, 3984, 716-718, doi:10.1126/science.172.3984.716.
- Behar, E., H. Nilsson, G. Stenberg-Wieser, Z. Nemeth, T. W. Broiles, and I. Richter (2015), Mass loading at 67P/Churyumov-Gerasimenko: a case study, *Geophys. Res. Lett.*, under revision.
- Behrigh, R., W. Eckstein, P. Meischner, B. M. U. Scherzer, and H. Verbeek (1975), Charged fraction of 5 keV to 150 keV hydrogen atoms after emergence from different metal surfaces, in *Atomic Collisions in Solids*, edited by S. Datz et al., Springer Science and Business Media New York, doi:10.1007/978-1-4684-3117-9_29.
- Benna, M., P. R. Mahaffy, J. S. Halekas, R. C. Elphic, and G. T. Delory (2015), Variability of helium, neon, and argon in the lunar exosphere as observed by the LADEE NMS instrument, *Geophys. Res. Lett.*, 42, 10, 3723-3729, doi:10.1002/2015GL064120.
- Benson, J., J. W. Freeman, H. K. Hills, and R. R. Vondrak (1975), Bow shock protons in the lunar environment, *The Moon*, 14, 1, 19-25, doi:10.1007/BF00562969.
- Biermann, L. (1951), Kometeschwerfe und solare Korpuskularstrahlung, *Z. Astrophys.*, 29:274.
- Binder, A. B. (1998), Lunar Prospector: Overview, *Science*, 281, 5382, 1475-1476, doi:10.1126/science.281.5382.1475.

- Blewett, D. T., E. I. Coman, B. R. Hawke, J. J. Gillis-Davis, M. E. Purucker, and C. G. Hughes (2011), Lunar swirls: Examining crustal magnetic anomalies and space weathering trends, *J. Geophys. Res.*, **116**, E02002, doi:10.1029/2010JE003656.
- Bochsler, P. (2000), Solar wind composition, *Encycl. Astronomy Astrophys.*, **1**, doi:10.1888/0333750888/2303.
- Borisov, N., and U. Mall (2003), Interaction of the solar wind with a localized magnetic barrier: application to lunar surface magnetic fields, *Phys. Lett. A.*, **309**, 277-289, doi:10.1016/S0375-9601(02)01655-9.
- Bosqued, J. M., et al. (1996), Moon-solar wind interactions: First results from the WIND/3DP experiment, *Geophys. Res. Lett.*, **23**, 10, 1259-1262, doi:10.1029/96GL00303.
- Bridge, H. S., C. Dilworth, A. J. Lazarus, E. F. Lyon, B. Rossi, and F. Scherb (1962), Direct observations of the interplanetary plasma, *J. Phys. Soc. Japan*, **17**, Supplement A-II.
- Burke, D. J., C. A. Dukes, J.-H. Kim, J. Shi, M. Famá, and R. A. Baragiola (2011), Solar wind contribution to surficial lunar water: Laboratory investigations, *Icarus*, **211**, 1082-1088, doi:10.1016/j.icarus.2010.11.007.
- Chapman, S., and V. C. A. Ferraro (1930), A new theory of magnetic storms, *Nature*, **126**, 129-130.
- Clay, D. R., B. E. Goldstein, M. Neugebauer, and C. W. Snyder (1975), Lunar surface solar wind observations at the Apollo 12 and Apollo 15 sites, *J. Geophys. Res.*, **80**, 13, 1751-1760, doi:10.1029/JA080i013p01751.
- Colburn, D. S., R. G. Currie, J. D. Mihalov, and C. P. Sonett (1967), Diamagnetic solar-wind cavity discovered behind Moon, *Science*, **158**, 1040, doi:10.1126/science.158.3804.1040.
- Colburn, D. S., J. D. Mihalov, and C. P. Sonett (1971), Magnetic observations of the lunar cavity, *J. Geophys. Res.*, **76**, 2940, doi:10.1029/JA076i013p02940.
- Coleman, P. J., Jr., G. Schubert, C. T. Russell, and L. R. Sharp (1972), Satellite measurements of the moon's magnetic field: A preliminary report, *The moon*, **4**, 3, 419-429, doi:10.1007/BF00562008.
- Collier, M. R., H. K. Hills, T. J. Stubbs, J. S. Halekas, G. T. Delory, J. Espley, W. M. Farrell, J. W. Freeman, and R. Vondrak (2011), Lunar surface electric potential

- changes associated with traversals through the Earth's foreshock, *Planet. Space Sci.*, 59, 14, 1727-1743, doi:10.1016/j.pss.2010.12.010.
- Criswell, D. R. (1972), Photoelectrons and solar wind/lunar limb interaction, *The moon*, 7, 1, 202-238, doi:10.1007/BF00578817.
- Deca, J., A. Divin, G. Lapenta, B. Lembége, S. Markidis, and M. Horányi (2014), Electromagnetic particle-in-cell simulations of the solar wind interaction with lunar magnetic anomalies, *Phys. Rev. Lett.*, 112, 151102, doi:10.1103/PhysRevLett.112.151102.
- Dhanya, M. B., A. Bhardwaj, Y. Futaana, S. Fatemi, M. Holmström, S. Barabash, M. Wieser, P. Wurz, A. Alok, and R. S. Thampi (2013), Proton entry into the near-lunar plasma wake for magnetic field aligned flow, *Geophys. Res. Lett.*, 40, 12, 2913-2917, doi:10.1002/grl.50617.
- Dolginov, S. S., Yeroshenko, Y. G., Zhuzgov, L. N., and Pushkov, N. V. (1961), Investigation of the magnetic field of the Moon, *Geomagnetism and Aeronomy*, 1, 18.
- Draxler, M., S. P. Chenakin, S. N. Markin, and P. Bauer (2005), Apparent velocity threshold in the electronic stopping of slow hydrogen ions in LiF, *Phys. Rev. Lett.*, 95, 113201, doi:10.1103/PhysRevLett.95.113201.
- Dyal, P., C. W. Parkin, and C. P. Sonett (1970), Apollo 12 Magnetometer: Measurement of a steady magnetic field on the surface of the Moon, *Science*, 169, 3947, 762-764, doi:10.1126/science.169.3947.762.
- Dyal, P., Parkin, C. W., Sonett, C. P., and Daily, W. D. (1974), Magnetism and the interior of the Moon, *Proc. 3rd Lunar Sci. Conf.*, p.2271-2286.
- Eastwood, J. P., E. A. Lucek, C. Mazelle, K. Mezaine, Y. Narita, J. Pickett, and R. A. Treumann (2005), The foreshock, in *Outer Magnetospheric Boundaries: Cluster Results*, edited by G. Paschmann, S. J. Schwartz, C. P. Escoubet, and S. Haaland, 41-94, 10.1007/1-4020-4582-4_3.
- Eckstein, W. (1981), Charge fractions of reflected particles, in *Inelastic Particle-Surface Collisions*, 157-183, Springer, Berlin Heidelberg.
- Fairfield, D. H. (1971), Average and unusual locations of the Earth's magnetopause and bow shock, *J. Geophys. Res.*, 76, 6700-6716, doi:10.1029/JA076i028p06700.

- Farrell, W. M., T. J. Stubbs, J. S. Halekas, R. M. Killen, G. T. Delory, M. R. Collier, and R. R. Vondrak (2010), Anticipated electrical environment within permanently shadowed lunar craters, *J. Geophys. Res. Planets*, **115**, E3, doi:10.1029/2009JE003464.
- Fatemi, S., M. Holmström, Y. Futaana, S. Barabash, and C. Lue (2013), The lunar wake current systems, *Geophys. Res. Lett.*, **40**, 17-21, doi:10.1029/2012GL054635
- Fatemi, S., M. Holmström, Y. Futaana, C. Lue, M. R. Collier, S. Barabash, and G. Stenberg (2014), Effects of protons reflected by lunar crustal magnetic fields on the global lunar plasma environment, *J. Geophys. Res. Space Physics*, **119**, 6095–6105, doi:10.1002/2014JA019900.
- Fatemi, S., C. Lue, M. Holmström, A. R. Poppe, M. Wieser, S. Barabash, and G. T. Delory (2015a), Solar wind plasma interaction with Gerasimovich lunar magnetic anomaly, *J. Geophys. Res., Space Physics*, **120**, 6, 4719-4735, doi:10.1002/2015JA021027.
- Fatemi, S., H. A. Fuqua, A. R. Poppe, G. T. Delory, J. S. Halekas, W. M. Farrell, and M. Holmström (2015b), On the confinement of lunar induced magnetic fields, *Geophys. Res. Lett.*, **42**, 17, 6931-6938, doi:10.1002/2015GL065576.
- Formisano, V., G. Moreno, F. Palmiotto, and P. C. Hedgecock (1973), Solar wind interaction with the Earth's magnetic field 1. Magnetosheath, *J. Geophys. Res.*, **78**, 19, doi:10.1029/JA078i019p03714.
- Frank, L. A. (1985), Plasmas in the earth's magnetotail, *Space Sci. Rev.*, **42**, 1, 211-240, doi:10.1007/BF00218233.
- Freeman, J. W., Jr. (1972), Energetic ion bursts on the nightside of the Moon, *J. Geophys. Res.*, **77**, 1, 239-243, doi:10.1029/JA077i001p00239.
- Freeman, J. W., Jr., M. A. Fenner, and H. K. Hills (1973), Electric potential of the Moon in the solar wind, *J. Geophys. Res.*, **78**, 22, doi:10.1029/JA078i022p04560.
- Futaana, Y., S. Machida, Y. Saito, A. Matsuoka, and H. Hayakawa (2003), Moon-related nonthermal ions observed by Nozomi: Species, sources, and generation mechanisms, *J. Geophys. Res.*, **108**, A1, 1025, doi:10.1029/2002JA009366.

- Futaana, Y., S. Barabash, M. Holmström, and A. Bhardwaj (2006), Low energy neutral atoms imaging of the Moon, *Planet. Space Sci.*, *54*, 2, 132-143, doi:10.1016/j.pss.2005.10.010.
- Futaana, Y., S. Barabash, M. Wieser, M. Holmström, A. Bhardwaj, M. B. Dhanya, R. Sridharan, P. Wurz, A. Schaufelberger, and K. Asamura (2010), Protons in the near-lunar wake observed by the Sub-keV Atom Reflection Analyzer on board Chandrayaan-1, *J. Geophys. Res.*, *115*, A10248, doi:10.1029/2010JA015264.
- Futaana, Y., S. Barabash, M. Wieser, M. Holmström, C. Lue, P. Wurz, A. Schaufelberger, A. Bhardwaj, M. B. Dhanya, and K. Asamura (2012), Empirical energy spectra of neutralized solar wind protons from the lunar regolith, *J. Geophys. Res.*, *117*, E05005, doi:10.1029/2011JE004019.
- Futaana, Y., S. Barabash, M. Wieser, C. Lue, P. Wurz, A. Vorburger, A. Bhardwaj, and K. Asamura (2013), Remote energetic neutral atom imaging of electric potential over a lunar magnetic anomaly, *Geophys. Res. Lett.*, *40*, 262-266, doi:10.1002/grl.50135.
- Garrick-Bethell, I., J. W. Head, III, and C. M. Pieters (2011), Spectral properties, magnetic fields, and dust transport at lunar swirls, *Icarus*, *212*, 480-492, doi:10.1016/j.icarus.2010.11.036.
- Giordano, L., J. Goniakowski, and G. Pacchioni (2003), Properties of MgO(100) ultrathin layers on Pd(100): Influence of the metal support, *Phys. Rev. B.*, *67*, 4, doi:10.1103/PhysRevB.67.045410.
- Gringauz, K. I., V. V. Bezrukh, V. D. Ozerov, and R. E. Ribchinsky (1961), Some results of experiments in interplanetary space by means of charged particle traps on Soviet space probes, *Space Res.*, *2*, 539-553.
- Goswami, J. N. and M. Annadurai (2008), Chandrayaan-1 mission to the Moon, *Acta Astronautica*, *63*, 11-12, 1215-1220, doi:10.1016/j.actaastro.2008.05.013.
- Greenstadt, E. W. (1971a), Conditions for magnetic interaction of asteroids with the solar wind, *Icarus*, *14*, 374-381, doi:10.1016/0019-1035(71)90008-X.
- Greenstadt, E. W. (1971b), Possible magnetic interaction of asteroids with the solar wind, in *Physical Studies of Minor Planets*, edited by T. Gehrels, NASA SP 267, 567-575, 1971NASSP.267..567G.

- Halekas, J. S., D. L. Mitchell, R. P. Lin, S. Frey, L. L. Hood, M. H. Acuña, and A. B. Binder (2001), Mapping of crustal magnetic anomalies on the lunar near side by the Lunar Prospector electron reflectometer, *J. Geophys. Res.*, *106*, E11, 27841-27852, doi:10.1029/2000JE001380.
- Halekas, J. S., D. A. Brain, D. L. Mitchell, R. P. Lin, and L. Harrison (2006), On the occurrence of magnetic enhancements caused by solar wind interaction with lunar crustal fields, *Geophys. Res. Lett.*, *33*, L08106, doi:10.1029/2006GL025931.
- Halekas, J. S., G. T. Delory, D. A. Brain, R. P. Lin, and D. L. Mitchell (2008), Density cavity observed over a strong lunar crustal magnetic anomaly in the solar wind: A mini-magnetosphere?, *Planet. Space Sci.*, *56*, 7, 941-946, doi:10.1016/j.pss.2008.01.008.
- Halekas, J. S., G. T. Delory, R. P. Lin, T. J. Stubbs, and W. M. Farrell (2009), Lunar Prospector measurements of secondary electron emission from lunar regolith, *Planet. Space Sci.*, *57*, 78-82, doi:10.1016/j.pss.2008.11.009.
- Halekas, J. S., R. J. Illis, R. P. Lin, M. Manga, M. E. Purucker, and R. A. Carley (2010), How strong are lunar crustal magnetic fields at the surface?: Considerations from a reexamination of the electron reflectometry technique, *J. Geophys. Res.*, *115*, E03006, doi:10.1029/2009JE003516.
- Halekas, J. S., Y. Saito, G. T. Delory, and W. M. Farrell (2011), New views of the lunar plasma environment, *Planet. Space Sci.*, *59*, 14, 1681-1694, doi:10.1016/j.pss.2010.08.011.
- Halekas, J. S. et al. (2012), Lunar precursor effects in the solar wind and terrestrial magnetosphere, *J. Geophys. Res. Space Physics*, *117*, A5, doi:10.1029/2011JA017289.
- Halekas, J. S., A. R. Poppe, and J. P. McFadden (2014), The effects of solar wind velocity distributions on the refilling of the lunar wake: ARTEMIS observations and comparisons to one-dimensional theory, *J. Geophys. Res., Space Physics*, *119*, 7, 5133-5149, doi:10.1002/2014JA020083.
- Harnett, E., and R. Winglee (2000), Two dimensional MHD simulation of the solar wind interaction with magnetic field anomalies on the surface of the Moon, *J. Geophys. Res.*, *105*, 24,997-25,007, doi:10.1029/2000JA000074.
- Harnett, E., and R. Winglee (2002), 2.5-D particle and MHD simulation of mini-magnetospheres at the Moon, *J. Geophys. Res.*, *107*, A12, 1421, doi:10.1029/2002JA009241.

- Harnett, E. M., and R. M. Winglee (2003a), 2.5-D fluid simulations of the solar wind interacting with multiple dipoles on the surface of the Moon, *J. Geophys. Res.*, **108**, A2, 1088, doi:10.1029/2002JA009617.
- Harnett, E. M., and R. M. Winglee (2003b), The influence of a mini-magnetopause on the magnetic pileup boundary at Mars, *Geophys. Res. Lett.*, **30**, 20, doi:10.1029/2003GL017852.
- Hinton, F. L., and D. R. Taeusch (1964), Variation of the lunar atmosphere with the strength of the solar wind, *J. Geophys. Res.*, **69**, 7, 1341-1347, doi:10.1029/JZ069i007p01341.
- Hodges, R. R. (2011), Resolution of the lunar hydrogen enigma, *Geophys. Res. Lett.*, **38**, L06201, doi:10.1029/2011GL046688.
- Hodges, R. R., and J. H. Hoffman (1975), Implications of atmospheric Ar escape on the interior structure of the Moon, *Proc. 6th Lunar Sci. Conf.*, 3039-3047.
- Holmström, M. (2010) Hybrid modeling of plasmas, in *Numerical Mathematics and Advanced Applications 2009*, edited by G. Kreiss, P. Lötstedt, A. Målqvist, and M. Neytcheva, 451-458, doi:10.1007/978-3-642-11795-4_48.
- Holmström, M., M. Wieser, S. Barabash, Y. Futaana, and A. Bhardwaj (2010), Dynamics of solar wind protons reflected by the Moon, *J. Geophys. Res.*, **115**, A06206, doi:10.1029/2009JA014843.
- Holmström, M., S. Fatemi, Y. Futaana, and H. Nilsson (2012), The interaction between the Moon and the solar wind, *Earth Planets Space*, **64**, 237-245, doi:10.5047/eps.2011.06.040.
- Holmström, M., and X.-D. Wang (2015), Mars as a comet: Solar wind interaction on a large scale, *Planet. Space Sci.*, *in press*, doi:10.1016/j.pss.2015.09.017.
- Hood, L. L. (1986), Geophysical constraints on the lunar interior, in *Origin of the Moon*, edited by W. K. Hartmann, R. J. Philips, and G. J. Taylor, Lunar and Planet. Inst., p. 361-410.
- Hood, L. L., A. Zakharian, J. Halekas, D. L. Mitchell, R. P. Lin, M. H. Acuña, and A. B. Binder (2001), Initial mapping and interpretation of lunar crustal magnetic anomalies using Lunar Prospector magnetometer data, *J. Geophys. Res.*, **106**(E11), 27825–27839, doi:10.1029/2000JE001366.
- Hundhausen, A. J. (1995), The solar wind, in *Introduction to Space Physics*, edited by M. G. Kivelson and C. T. Russell, 96-110, Cambridge University Press.

- Johnson, F. S. (1971), Lunar atmosphere, *Rev. Geophys.*, 9, 3, 813-823, doi:10.1029/RG009i003p00813.
- Johnson, R. E. and R. Baragiola (1991), Lunar surface: Sputtering and secondary ion mass spectrometry, *Geophys. Res. Lett.*, 18, 11, 2169-2172, doi:10.1029/91GL02095.
- Johnson, F. S., J. M. Carroll, and D. E. Evans (1972), Lunar atmosphere measurements, *Proc. 3rd Lunar Sci. Conf.*, 3, 2231-2242.
- Joliff, B. L., J. J. Gillis, L. Haskin, R. L. Korotev, and M. A. Wieczorek (2000), Major lunar crustal terranes: Surface expressions and crust-mantle origins, *J. Geophys. Res.*, 105, E2, 4197-4216, doi:10.1029/1999JE001103.
- Kallio, E., R. Jarvinen, S. Dyadechkin, P. Wurz, S. Barabash, F. Alvarez, V. A. Fernandes, Y. Futaana, A.-M. Harri, J. Heilimo, C. Lue, J. Mäkelä, N. Porjo, W. Schmidt, and T. Siili (2012), Kinetic simulations of finite gyroradius effects in the lunar plasma environment on global, meso, and microscales, *Planet. Space Sci.*, 74, 1, 146-155, doi:10.1016/j.pss.2012.09.012.
- Kato, M., S. Sasaki, Y. Takizawa, and the Kaguya project team (2010), The Kaguya Mission Overview, *Space Sci. Rev.*, 154, 3-19, doi:10.1007/s11214-010-9678-3.
- Kazama, Y., S. Barabash, A. Bhardwaj, K. Asamura, Y. Futaana, M. Holmström, R. Lundin, R. Sridharan, and P. Wurz (2006), Energetic neutral atom imaging mass spectroscopy of the Moon and Mercury environments, *Adv. Space Res.*, 37, 38-44, doi:10.1016/j.asr.2005.05.047.
- Kellogg, P. J., K. Goetz, S. J. Monson, J.-L. Bougeret, R. Manning, and M. L. Kaiser (1996), Observations of plasma waves during a traversal of the moon's wake, *Geophys. Res. Lett.*, 23, 10, 1267-1270, doi:10.1029/96GL00376.
- Kramer, Y. G. et al. (2011a), M³ spectral analysis of lunar swirls and the link between optical maturation and surface hydroxyl formation at magnetic anomalies, *J. Geophys. Res. Planets*, 116, E9, doi:10.1029/2010JE003729.
- Kramer, Y. G., J.-P. Combe, E. M. Harnett, B. R. Hawke, S. K. Noble, D. T. Blewett, T. B. McCord, and T. A. Giguere (2011b), Characterization of lunar swirls at Mare Ingenii: A model for space weathering at magnetic anomalies, *J. Geophys. Res.*, 116, E04008, doi:10.1029/2010JE003669.

- Lawrence, D. J., W. C. Feldman, B. L. Barraclough, A. B. Binder, R. C. Elphic, S. Maurice, and D. R. Thomsen (1998), Global elemental maps of the Moon: The Lunar Prospector gamma-ray spectrometer, *Science*, **281**, 1484-1489.
- Lin, R. P., D. L. Mitchell, D. W. Curtis, K. A. Anderson, C. W. Carlson, J. McFadden, M. H. Acuña, L. L. Hood, and A. Binder (1998), Lunar surface magnetic fields and their interaction with the solar wind: Results from Lunar Prospector, *Science*, **281**, 1480-1484, doi:10.1126/science.281.5382.1480.
- Lucas, A. A. (1973), Fundamental processes in particle and photon interactions with surfaces, in *Photon and Particle Interactions with Surfaces in Space*, edited by R. J. L. Garard, D. Reidel Publishing Company, Dordrecht-Holland/Boston-U.S.A. ISBN 90 277 0381 7.
- Lue, C., Y. Futaana, S. Barabash, M. Wieser, M. Holmström, A. Bhardwaj, M. B. Dhanya, and P. Wurz (2011), Strong influence of lunar crustal fields on the solar wind flow, *Geophys. Res. Lett.*, **38**, L03202, doi:10.1029/2010GL046215.
- Lue, C., Y. Futaana, S. Barabash, M. Wieser, A. Bhardwaj, and P. Wurz (2014), Chandrayaan-1 observations of backscattered solar wind protons from the lunar regolith: Dependence on the solar wind speed, *J. Geophys. Res. Planets*, **119**, 968-975, doi:10.1002/2013JE004582.
- Lue, C., Y. Futaana, S. Barabash, Y. Saito, M. Nishino, M. Wieser, K. Asamura, A. Bhardwaj, and P. Wurz (2015a), Scattering characteristics and imaging of energetic neutral atoms from the Moon in the terrestrial magnetosheath, *J. Geophys. Res.*, under revision.
- Lue, C., Y. Futaana, S. Barabash, M. Wieser, A. Bhardwaj, P. Wurz, and K. Asamura (2015b), Solar wind scattering from the surface of Mercury: Lessons from the Moon, in preparation.
- Luhmann, J. G. (1995), Plasma interactions with unmagnetized bodies, in *Introduction to Space Physics*, edited by M. G. Kivelson and C. T. Russell, 203-225.
- Lyon, E. F., H. S. Bridge, and J. H. Binsack (1967), Explorer 35 plasma measurements in the vicinity of the Moon, *J. Geophys. Res.*, **72**, 6113, doi:10.1029/JZ072i023p06113.
- Massey, H. S. W. (1950), *Negative ions*, 2nd ed., Cambridge University Press.
- Massey, H. S. W. and E. H. S. Burhop (1952), *Electronic and ionic impact phenomena*, Oxford University Press.

- McCann, D., S. Barabash, H. Nilsson, and A. Bhardwaj (2007), Miniature ion mass analyzer, *Planet. Space Sci.*, *55*, 1190-1196, doi:10.1016/j.pss.2006.11.020.
- McComas, D. J., et al. (2009), Lunar backscatter and neutralization of the solar wind: First observations of neutral atoms from the Moon, *Geophys. Res. Lett.*, *36*, L12105, doi:10.1029/2009GL038794.
- Mihalov, J. D., C. P. Sonett, J. H. Binsack, and M. D. Moutsoulas (1971), Possible fossil lunar magnetism inferred from satellite data, *Science*, *171*, 3974, 892-895, doi:10.1126/science.171.3974.892.
- Nakagawa, T., Y. Takahashi, and M. Iizima (2003), Geotail observation of upstream ULF waves associated with lunar wake, *Earth Planets Space*, *55*, 596-580, doi:10.1186/BF03351789.
- Neugebauer, M., C. W. Snyder, D. R. Clay, and B. E. Goldstein (1972), Solar wind observations on the lunar surface with the Apollo 12 ALSEP, *Planet. Space Sci.*, *20*, 1577-1591, doi:10.1016/0032-0633(72)90184-5.
- Ness, N. F., K. W. Behannon, C. S. Scarce, and S. C. Cantarano (1967), Early results from the magnetic field experiment on Lunar Explorer 35, *J. Geophys. Res.*, *72*, 5769, doi:10.1029/JZ072i023p05769.
- Ness, N. F., K. W. Behannon, H. E. Taylor, and Y. C. Whang (1968), Perturbations of the interplanetary magnetic field by the lunar wake, *J. Geophys. Res.*, *73*, 3421, doi:10.1029/JA073i011p03421.
- Ness, N. F. (1969), The geomagnetic tail, *Rev. Geophys.*, *7*, 1-2, 97-127, doi:10.1029/RG007i001p00097.
- Niehus, H., W. Heiland, and E. Taglauer (1993), Low-energy ion scattering at surfaces, *Surf. Sci. Rep.*, *17*, 4-5, 213-303, doi:10.1016/0167-5729(93)90024-J.
- Nishino, M. N., et al. (2009), Solar-wind proton access deep into the near-Moon wake, *Geophys. Res. Lett.*, *36*, L16103, doi:10.1029/2009GL039444.
- Nozette, S. et al. (1994), The Clementine mission to the moon: Scientific overview, *Science*, *266*, 5192, 1835.
- Ogilvie, K. W. and M. D. Desch (1997), The wind spacecraft and its early scientific results, *Adv. Space Res.*, *20*, 4, 559-568, doi:10.1016/S0273-1177(97)00439-0.

- Ogilvie, K. W., J. T. Steinberg, R. J. Fitzenreiter, C. J. Owen, A. J. Lazarus, W. M. Farrell, and R. B. Torbert (1996), Observations of the lunar plasma wake from the WIND spacecraft on December 27, 1994, *Geophys. Res. Lett.*, **23**, 10, 1255-1258, doi:10.1029/96GL01069.
- Omidi, N., X. Blanco-Cano, C. T. Russell, H. Harimabadi, and M. Acuna (2002), Hybrid simulations of solar wind interaction with magnetized asteroids: General characteristics, *J. Geophys. Res.*, **107**, A12, 1487, doi:10.1029/2002JA009441.
- Parker, E. N. (1958), Dynamics of the interplanetary gas and magnetic fields, *Astrophys. J.*, **128**, 664.
- Parker, E. N. (1963), Interplanetary dynamical processes, *New York, Interscience Publishers*, 1963, 1.
- Poppe, A. R., J. S. Halekas, G. T. Delory, and W. M. Farrell (2012), Particle-in-cell simulations of the solar wind interaction with lunar crustal magnetic anomalies: Magnetic cusp regions, *J. Geophys. Res.*, **117**, A09105, doi:10.1029/2012JA017844.
- Purucker, M. E. (2008), A global model of the internal magnetic field of the Moon based on Lunar Prospector magnetometer observations, *Icarus*, **197**, 19-23, doi:10.1126/science.1178658.
- Purucker, M. E., and J. B. Nicholas (2010), Global spherical harmonic models of the internal magnetic field of the Moon based on sequential and coestimation approaches, *J. Geophys. Res.*, **115**, E12007, doi:10.1029/2010JE003650.
- Reasoner, D. L. and W. J. Burke (1972), Direct observation of the lunar photoelectron layer, *Proc. 3rd Lunar Sci. Conf.*, **3**, 2639-2654, The M.I.T. Press.
- Rich, F. J., D. L. Reasoner, and W. J. Burke (1973), Plasma sheet at lunar distance: Characteristics and interactions with the lunar surface, *J. Geophys. Res.*, **78**, 34, doi:10.1029/JA078i034p08097.
- Russell, C. T. (1995), A brief history of solar-terrestrial physics, in *Introduction to Space Physics*, edited by M. G. Kivelson and C. T. Russell.
- Russell, C. T., Coleman, P. J. Jr., and Schubert, G. (1974), Lunar magnetic fields: Permanent and induced dipole moments, *Science*, **186**, 825.
- Russell, C. T., Coleman, P. J., and Goldstein, B. E. (1981), Magnetic evidence for a lunar core, *Proc. 12th Lunar and Planet. Sci. Conf.*

- Russell, C. T., and B. R. Lichtenstein (1975), On the source of lunar limb compressions, *J. Geophys. Res.*, **80**, 4700-4711, doi:10.1029/JA080i034p04700.
- Sadovskii, A., and A. Skalsky (2014), Coupling of earth's magnetosphere, solar wind and lunar plasma environment, *Adv. Space Res.*, **54**, 10, 2017-2020, doi:10.1016/j.asr.2013.07.028.
- Saito, Y., et al. (2008), Solar wind proton reflection at the lunar surface: Low energy ion measurement by MAP-PACE onboard SELENE (KAGUYA), *Geophys. Res. Lett.*, **35**, L24205, doi:10.1029/2008GL036077.
- Saito, Y., et al. (2010) In-flight performance and initial results of Plasma Energy Angle and Composition Experiment (PACE) on SELENE (Kaguya), *Space Sci. Rev.*, **154**, 1, 265-303, doi:10.1007/s11214-010-9647-x.
- Saito, Y., et al. (2012), Simultaneous observation of the electron acceleration and ion deceleration over lunar magnetic anomalies, *Earth Planets Space*, **64**, 83-92, doi:10.5047/eps.2011.07.011.
- Schaufelberger, A., P. Wurz, S. Barabash, M. Wieser, Y. Futaana, M. Holmström, A. Bhardwaj, M. B. Dhanya, R. Sridharan, and K. Asamura (2011), Scattering function for energetic neutral hydrogen atoms off the lunar surface, *Geophys. Res. Lett.*, **38**, L22202, doi:10.1029/2011GL049362.
- Schwabe, H. (1843), Solar observations during 1843, *Astronomische Nachrichten*, **20**, 495, 234-235.
- Shaikhislamov, I. F., Yu. P. Zakharov, V. G. Posukh, A. V. Melekhov, V. M. Antonov, E. L. Boyarintsev, and A. G. Ponomarenko (2014), Experimental study of a mini-magnetosphere, *Plasma Phys. Controlled Fusion*, **56**, 2, doi:10.1088/0741-3335/56/2/025004.
- Shue, J.-H., J. K. Chao, H. C. Fu, C. T. Russell, P. Song, K. K. Khurana, and H. J. Singer (1997), A new functional form to study the solar wind control of the magnetopause size and shape, *J. Geophys. Res.*, **102**, 9497-9511, doi:10.1029/97JA00196.
- Sidorov, A. N., et al. (2011) Thermoelectric power of graphene as surface charge doping indicator, *Appl. Phys. Lett.*, **99**, 013115, doi:10.1063/1.3609858.
- Smith, J. V., A. T. Anderson, R. C. Newton, E. J. Olsen, P. J. Wyllie, A. V. Crewe, M. S. Isaacson, and D. Johnson (1970), Petrologic history of the Moon inferred

- from petrography, mineralogy, and petrogenesis of Apollo 11 rocks, *Proc. Apollo 11 Lunar Sci. Conf.*, Pergamon Press, 897-925.
- Snowden, S. L., M. R. Collier, and K. D. Kuntz (2004), XMM-Newton observation of solar wind charge exchange emission, *Astrophys. J.*, **610**, 2, doi:10.1086/421841.
- Sonett, C. P., D. S. Colburn, and R. G. Currie (1967), The intrinsic magnetic field of the Moon, *J. Geophys. Res.*, **72**, 21, 5503-5507, doi:10.1029/JZ072i021p05503.
- Spreiter, J. R., M. C. Marsh, and A. L. Summers (1970), Hydromagnetic aspects of solar wind flow past the Moon, *Cosmic Electrodyn.*, **1**, 5-50.
- Starukhina, L. V. (2003), Computer simulations of sputtering of lunar regolith by solar wind protons: Contribution to change of surface composition and to hydrogen flux at the lunar poles, *Solar System Res.*, **37**, 1, 36-50, doi: 10.1023/A:1022347821862.
- Stern, S. A. (1999), The lunar atmosphere: History, status, current problems, and context, *Rev. Geophys.*, **37**, 4, 453-491, doi:10.1029/1999RG900005.
- Stern, S. A., J. C. Cook, J.-Y. Chaufray, P. D. Feldman, G. R. Gladstone, and K. D. Retherford (2013), *Icarus*, **226**, 2, 1210-1213, doi:10.1016/j.icarus.2013.07.011.
- Stubbs, T. J., R. R. Vondrak, and W. M. Farrell (2006), A dynamic fountain model for lunar dust, *Adv. Space Res.*, **37**, 1, 59-66, doi:10.1016/j.asr.2005.04.048.
- Taylor, L. A., and Y. Liu (2010), Important considerations for lunar soil simulants, *Earth and Space 2010*, 106-118, doi:10.1061/41096(366)14.
- Tsunakawa, H., H. Shibuya, F. Takahashi, H. Shimizu, M. Matsushima, A. Matsuoka, S. Nakazawa, H. Otake, Y. Iijima (2010), Lunar magnetic field observation and initial global mapping of lunar magnetic anomalies by MAP-LMAG onboard SELENE (Kaguya), *Space Sci. Rev.*, **154**, 1, 219-251, doi:10.1007/s11214-010-9652-0.
- Verbeek, H., W. Eckstein, and S. Datz (1976), Positive and negative hydrogen ions backscattered from Au, Ta, and ThO₂ in the energy range up to 15 keV, *J. Appl. Phys.*, **47**, 1785, doi:10.1063/1.322892.

- Vorburger, A., P. Wurz, S. Barabash, M. Wieser, Y. Futaana, M. Holmström, A. Bhardwaj, and K. Asamura (2012), Energetic neutral atom imaging of the lunar surface, *J. Geophys. Res.*, **117**, A07208, doi:10.1029/2012JA017553.
- Vorburger, A., P. Wurz, S. Barabash, M. Wieser, Y. Futaana, C. Lue, M. Holmström, A. Bhardwaj, M. B. Dhanya, and K. Asamura (2013), Energetic neutral atom imaging of the lunar surface, *J. Geophys. Res. Space Physics*, **118**, 3937-3945, doi:10.1002/jgra.50337.
- Vorburger, A., P. Wurz, S. Barabash, M. Wieser, Y. Futaana, A. Bhardwaj, and K. Asamura (2015), Imaging the South Pole-Aitken basin in backscattered neutral hydrogen atoms, *Planet. Space Sci.*, **115**, 57-63, doi:10.1016/j.pss.2015.02.007.
- Wagner, S. A. (2006), The Apollo Experience Lessons Learned for Constellation Lunar Dust Management, *NASA Technical Publication TP-2006-213726*, Washington, DC: National Aeronautics and Space Administration.
- Wang, X.-D., et al. (2010), Acceleration of scattered solar wind protons at the polar terminator of the Moon: Results from Chang'E-1/SWIDs, *Geophys. Res. Lett.*, **37**, L07203, doi:10.1029/2010GL042891.
- Wang, Y.-C., J. Müller, W.-H. Ip, and U. Motschmann (2011), A 3D hybrid simulation study of the electromagnetic field distributions in the lunar wake, *Icarus*, **216**, 415-425, doi:10.1016/j.icarus.2011.09.021.
- Wang, X., M. Horányi, and S. Robertson (2012), Characteristics of a plasma sheath in a magnetic dipole field: Implications to the solar wind interaction with the lunar magnetic anomalies, *J. Geophys. Res.*, **117**, A06226, doi:10.1029/2012JA017635.
- Wekhof, A. (1981), Negative ions in the ionospheres of planetary bodies without atmospheres, *The moon and the planets*, **24**, 2, pp.45-52., doi:10.1007/BF00897567.
- Wieczorek, M. A., et al. (2006), The constitution and structure of the lunar interior, *Rev. Mineral. Geochem.*, **60**, 221-364, doi: 10.2138/rmg.2006.60.3.
- Wiehle, S., et al. (2011), First lunar wake passage of ARTEMIS: Discrimination of wake effects and solar wind fluctuations by 3D hybrid simulations, *Planet. Space Sci.*, **59**, 661-671, doi:10.1016/j.pss.2011.01.012.
- Wieser, M., P. Wurz, K. Brünig, and W. Heiland (2002) Scattering of atoms and molecules off a magnesium oxide surface, *Nucl. Inst. Methods Phys. Res. B*:

Beam Interact. Mater. Atoms, 192, 4, pp.370-380, doi:10.1016/S0168-583X(02)00486-X.

Wieser, M., S. Barabash, Y. Futaana, M. Holmström, A. Bhardwaj, R. Sridharan, M. B. Dhanya, P. Wurz, A. Schaufelberger, and K. Asamura (2009), Extremely high reflection of solar wind protons as neutral hydrogen atoms from regolith in space, *Planet. Space Sci.*, 57, 14-15, doi:10.1016/j.pss.2009.09.012.

Wieser, M., S. Barabash, Y. Futaana, M. Holmström, A. Bhardwaj, R. Sridharan, M. B. Dhanya, A. Schaufelberger, P. Wurz, and K. Asamura (2010), First observation of a mini-magnetosphere above a lunar magnetic anomaly using energetic neutral atoms, *Geophys. Res. Lett.*, 37, L05103, doi:10.1029/2009GL041721.

Wood, J. A., J. S. Dickey, U. B. Marvin, and B. N. Powell (1970), Lunar anorthosites and a geophysical model of the Moon. *Proc. Apollo 11 Lunar Sci. Conf.*, Pergamon Press, 965-988.

Zimmerman, M. I., W. M. Farrell, and A. R. Poppe (2015), Kinetic simulations of kilometer-scale mini-magnetosphere formation on the Moon, *J. Geophys. Res.*, in Press, doi:10.1002/2015JE004865.